View metadata, citation and similar papers at core.ac.uk

brought to you by CORE

provided by NASA Technical Reports Server

NASA Technical Memorandum 101003

Flow-Field Survey of an Empennage Wake Interacting with a Pusher Propeller

W. Clifton Horne and Paul T. Soderman

(NASA-TM-101003) FLOW-FIELD SURVEY OF AN EMPENNAGE WAKE INTERACTING WITH A PUSHER PROPELLER (NASA) 54 p CSCL 01B

N89-11694

Unclas
G3/01 0174588

October 1988

National Aeronautics and Space Administration

NASA Technical Memorandum 101003

Flow-Field Survey of an Empennage Wake Interacting with a Pusher Propeller

W. Clifton Horne, Paul T. Soderman, Ames Research Center, Moffett Field, California

October 1988

National Aeronautics and
Space Administration

Ames Research Center
Moffett Field, California 94035

SUMMARY

The flow field between a model empennage and a 591-mm-diameter pusher propeller was studied in the Ames 7- by 10- Foot Wind Tunnel with directional pressure probes and hot-wire anemometers. The region probed was bounded by the empennage trailing edge and downstream propeller. The wake properties, including effects of propeller operation on the empennage wake, were investigated for two empennage geometries: one, a vertical tail fin, the other, a Y-tail with a 34° dihedral. Results showed that the effect of the propeller on the empennage wake upstream of the propeller was not strong. The flow upstream of the propeller was accelerated in the streamwise direction by the propeller, but the empennage wake width and velocity defect were relatively unaffected by the presence of the propeller. The peak turbulence in the wake near the propeller tip station, 0.66 diameter behind the vertical tail fin, was approximately 3 % of the free-stream velocity. The velocity field data can be used in predictions of the acoustic field due to propeller-wake interaction.

SYMBOLS

b	wake width measured at mid height of $\bar{U}_{max}$, mm
c	chord of airfoil, mm
C_t	thrust coefficient, thrust $/(\rho N^2 D^4)$
d	diameter of cylinder, mm
D	propeller diameter, m
f	frequency of disturbance in wake, Hz
ι	turbulent eddy length, mm
N	propeller rotation speed, rev/sec
T	period of disturbance in wake, sec/cycle
u'	unsteady streamwise velocity component in X direction (rms), m/sec
U	local mean streamwise velocity in X direction, m/sec
$\bar{U}$	normalized streamwise velocity in wake, $(U_\infty - U)/U_\infty$
$\bar{U}_{max}$	maximum normalized streamwise velocity in wake

U_∞ mean velocity in the free stream measured 1.3 m upstream of the fuselage nose, m/sec

v' unsteady velocity component in cross-stream Y direction (rms), m/sec

w' unsteady velocity in cross-stream Z direction (rms), mm

X coordinate downstream from aft tip of fuselage, mm

X' distance from local empennage trailing edge in X direction, mm

Y coordinate in vertical direction (upward) relative to fuselage centerline, mm

Z coordinate in cross-stream direction relative to fuselage centerline, to the right looking downstream, mm

β stream yaw angle between X axis and the projection of the streamline on the X-Z plane (positive β denotes a streamline with a positive Z component), deg

φ boundary-layer momentum thickness on one side of a flat plate at the trailing edge, mm

ρ air density, kg/m^3

θ stream pitch angle between the X axis and the projection of the streamline on the X-Y plane (positive downward), deg

INTRODUCTION

Propellers are common on general aviation and business aircraft and are being considered for new commercial aircraft designs because of the development of advanced, fuel-efficient propeller and propfan configurations. Consequently, there is a renewed interest in the alleviation of propeller noise. That noise is aggravated by unsteadiness and nonuniformity in the inflowing stream caused by atmospheric turbulence or propeller installation effects. Pusher-propeller configurations are particularly susceptible to the ingestion of wakes from wings, fuselages, or empennage surfaces. Although it is relatively easy to predict the mean velocity distribution in wakes from streamlined surfaces in the absence of a downstream propeller, the interaction of a wake with a propeller is complex if the propeller influences the wake and vice versa.

The purpose of this study was to measure the radiated noise and the inflow velocity field associated with a model-scale pusher propeller. The acoustic data are presented in a separate report (ref. 1). Further analysis of the data in reference 1 will be published by Soderman and Horne as a NASA numbered report. The results of the present study will support the development and verification of acoustic-source models, which require accurate specification of the inflow-velocity field with regard to the location and intensity of disturbances such as wakes. References 1 through 7 describe the type of acoustic effects caused by propeller/wake interactions, but the published flow-field data are quite limited. The velocity measurements reported in this study characterize the evolution of mean and turbulent velocities in wakes originating from

two different empennage surfaces, including the effects of propeller rotation on wake characteristics. The region of interest is between the empennage trailing edge and the downstream propeller.

EXPERIMENTAL METHOD

Test Facility and Model

Velocity and acoustic measurements were made in the Ames 7- by 10- Foot Wind Tunnel in an open-throat test section surrounded by an acoustically treated test hall shown in figures 1(a) through (d), which include photos of the various model configurations used in this study. The wind tunnel was operated at a constant flow speed of 46 m/sec, as measured with a pitot-static probe located 1.3 m upstream of the fuselage nose, 1.16 m above the floor, and 51 mm to the left of the duct centerline. The Reynolds number relative to the empennage chord at the propeller tip station ranged from 0.94×10^6 for the Y-tail to 1.4×10^6 for the vertical tail fin.

Tail surfaces were mounted upstream of the propeller on a movable fuselage model as illustrated in figures 2(a) and (b). The empennage and propeller were sized to match each other, but the fuselage was smaller than a typical fuselage. That is because the fuselage was available to support the empennage, and was not needed to simulate any particular configuration. The primary interest was in the empennage wake and not the fuselage wake. Therefore, the results are not greatly affected by the undersized fuselage. Empennage designs consisted of a Y-tail, including a dorsal fin, and a simple vertical tail fin shown in figures 3(a) and (b). Figure 3(c) shows the chord distributions. All empennage sections were NACA 0012 airfoils in the streamwise direction. That is, the symmetrical sections had a maximum thickness-to-chord ratio of 0.12, with the maximum thickness located at 30% chord. The Y-tail upper surfaces had a 34° dihedral and were set at 1° angle of attack. The sweep angle at the Y-tail leading edge was 22°. The vertical tail fin was at 0° angle of attack and had sweep angles at the leading edge, quarter-chord line, and trailing edge of 57°, 51°, and 32°, respectively. Both empennages were tapered.

The model propeller was a 591-mm diameter, four-bladed, unswept SR-2 configuration. It was mounted separately from the empennage to allow variations in propeller-empennage separation distance as shown in figures 2(a) and (b). For the data reported here, the propeller location was fixed at 573 mm downstream of the fuselage. The empennage/propeller distance varied from 383 mm to 573 mm depending on empennage sweep angle as described above. The propeller was mounted on a 711-mm-long shaft upstream of an electric motor in a nacelle. Rotation was counterclockwise looking upstream. This size of propeller and empennage would be approximately 1/3 to 1/5th scale of typical full-scale aircraft components. The data are presented nondimensionalized and should be representative of full-scale wakes. Figures 4(a) through (c) illustrate the propeller geometry. The hub diameter was 98 mm. The propeller chord was approximately 93 mm over much of the span. Reference 5 describes the SR-series propellers. Velocity surveys were carried out with the propeller either removed or installed and rotating at 8200 rpm, which gave a tip Mach number of 0.74. The helical Mach number at the tip was 0.76. Blade pitch angle at the 3/4 radius station was 16° relative to the disc plane. At a forward speed of 46 m/sec, the propeller advance ratio was 0.57 and the free-stream thrust coefficient, C_t, was estimated to be 0.05.

Test Instrumentation

Velocity sensors were mounted on a traversing mechanism located between the open-jet side shear layer (left side looking upstream) and the model. Figure 5 shows the survey rig installed in a closed test section for another study. It had three basic components: a lower table mounted on braces, a vertical traversing mechanism, and a horizontal survey strut which projected to the empennage wake. The vertical traversing mechanism holding the horizontal survey strut was about 1.0 m from the fuselage when the probes were in the empennage wake. The lower table was about 200 mm below the fuselage and 699 mm to the side of the fuselage. The horizontal survey strut containing the probes was 914 mm long. The four flow sensors in the survey strut included a pitot-static probe, a five-hole directional pressure probe, and two X-wire probes for turbulence measurements. Details of the probe assembly are shown in figure 6. The pressure-sensing probes were connected to individual pressure transducers and were calibrated in the wind tunnel to $\pm 30°$ stream angle. The X-wire probes were operated in the constant temperature mode and were calibrated against the wind-tunnel dynamic-pressure probe once every 3 to 4 surveys. Hot-wire signal fluctuations below 2 Hz were eliminated. Mean velocity measurements obtained from the hot wires agreed with pressure-probe measurements to within 7% and were operated without temperature compensation. A fixed pitot-static probe was used to measure test-section dynamic pressure upstream of the model.

Pressure transducer- and nonlinearized anemometer-output voltages were recorded with a computer-controlled data-acquisition system, which also controlled the positioning of the survey apparatus and probes. A schematic of the data-acquisition and reduction system is shown in figure 7. The system is capable of simultaneously sampling 15 data channels of random signals such as hot-wire voltages. Details of the data acquisition and reduction algorithms are given in the Appendix.

The empennage-wake velocity data were acquired during linear traverses consisting of uniformly-spaced survey points. Horizontal and vertical traverses at various downstream locations were obtained for each empennage configuration so as to characterize the mean and turbulent velocity fields.

Coordinate System and Survey Locations

The coordinate system and flow angles are shown in figure 8. The fixed coordinate system origin is the aft tip of the fuselage. In this system, the X axis is aligned with the horizontal uniform-stream velocity vector, and is positive downstream. The Y axis is directed upward, and the Z axis extends in the horizontal cross-stream direction to form a right-handed system (positive to the right looking downstream). The stream pitch angle, θ, denotes the angle between the X axis and the projection of the streamline on the X-Y plane, such that a positive θ denotes a descending streamline. The stream yaw angle, β, is the angle between the X axis and the projection of the streamline on the X-Z plane, and a positive β denotes a streamline with a positive Z component.

The vertical tail-fin trailing edge, propeller, and survey field are shown in figure 9. The locations where the cross-stream surveys crossed the wake center in the X-Y plane are noted. Propeller-off survey locations are shown as open circles, and propeller-on surveys are shown as "x" marks. The Y-tail trailing edge, propeller, and associated surveys are shown in figure 10, which is an upward view of the plane contiguous with the left surface of the Y-tail. The locations where the vertical surveys crossed the wake centers are noted.

Since wake development is a function of the distance downstream from an aerodynamic body, all velocity data are plotted relative to the empennage trailing edge. That distance measured in the horizontal plane is noted as X′. Since the vertical tail-fin trailing edge was swept, a probe location at a fixed wake distance, X′, might be relatively close or far from the (X, Y, Z) fuselage coordinate-system origin (see fig. 8).

RESULTS AND DISCUSSION

Mean Velocity Surveys

Vertical Tail Fin

A typical survey of the normalized streamwise-velocity deficit in the wake behind the vertical tail fin,

$$\bar{U} = \left(\frac{U_\infty - U}{U_\infty}\right) \tag{1}$$

is shown in figure 11, where U_∞ was the free-stream velocity measured upstream of the model, and U was measured in the wake. The data were acquired by using the pitot-static probe with the propeller blades removed from the hub. Traverses were made in the horizontal Z-direction 51 mm above the aft fuselage tip, and was approximately 25 mm above the base of the vertical tail fin. Traverses at streamwise locations relative to the aft fuselage tip of 3.8, 105, 215, and 316 mm are shown in figure 11. The wake profiles are shown as if the viewer were looking downstream. The data in figure 11 taken just downstream of the trailing edge (X′ = 3.8 mm) has the character of a finite flat plate near wake. The peak velocity deficit was $\bar{U} = 0.78$. At locations further downstream, the peak deficit was reduced to 0.23, and the tail-fin wake merged with the fuselage wake to form a broad wake. This broad wake was observed only low on the empennage, the traverse being only 51 mm above the fuselage centerline. At higher locations discussed below, the fuselage wake was not visible in the data. The asymmetry in the wake, shown by wake displacement relative to the Z origin, may be an effect of traverse-support blockage. It is likely that flow accelerations around the survey rig caused the fuselage wake to move slightly toward the survey rig. At higher stations above the large survey base structure, wake movement was very small. These surveys taken 51 mm above the fuselage center represent the portion of the wake ingested in the hub region of the propeller, a wake region not expected to affect the acoustic field significantly.

The effect of propeller rotation on the wake near the midspan of the tail fin (and propeller) is seen in figures 12(a) and (b), which illustrate wake behavior 203 mm above the fuselage (and propeller) centerlines at distances 5.6, 107, 209, and 310 mm downstream of the empennage trailing edge. The data of figure 12(a) were taken with the propeller removed from the hub, and the data with propeller operation (fig. 12(b)) were taken at a propeller rotational speed of 8200 rpm. Because the empennage was swept back, the propeller tip was only 383 mm from the empennage. The near wake had a similar character seen in the previous figure regardless of the absence or presence of the propeller. The wakes of the two figures remain similar until just upstream of the propeller where acceleration of the incoming stream from the propeller is apparent from the negative value of $\bar{U}$. (A negative value of the normalized velocity means that the local flow speed is greater than the free-stream velocity.) The wake is neither intensified, in the sense of a greater velocity defect, nor narrowed by the propeller by any large amount despite the acceleration in the near propeller field. That is, the wake velocity profiles are similar with the propeller operating and with the propeller off. (The apparent acceleration of the flow at the second location (X′ = 107 mm is probably anomalous.) The comparison of wake deficit with and without propeller operation is more

clearly seen in figure 12(c), which is an enlargement of the plots at $X' = 209$ mm. The flow acceleration by the propeller is clearly seen in terms of the downward shift of $\bar{U}$. But the shape and lateral location of the wake was virtually unchanged by the propeller.

A similar view of the wake ingested near the propeller tip is shown in figures 13(a) and (b) at a location 305 mm above the model centerline. (The propeller radius was 295 mm.) Downstream locations relative to the tail-fin trailing edge were 7.6, 109, 211, and 264 mm. Acceleration effects were negligible in this case. No significant wake displacement or intensification (velocity defect increase) by the propeller are evident in these surveys. In each of the surveys, the velocity deficit and wake widths measured with the propeller operating are similar to data at the same streamwise location, X', measured with the propeller off.

Figure 14 shows the wake character measured with horizontal surveys at a fixed streamwise location 103 mm upstream of the propeller disc and at four vertical stations. Propeller speed again was 8200 rpm. The fuselage wake is apparent in the data in the top plot measured 51 mm above the fuselage centerline. At higher stations, only the empennage wake is seen. Acceleration effects (negative $\bar{U}$) are seen at midspan locations of $Y = 102$ and 203 mm and disappear at the tip location, $Y = 305$ mm. Thus, the stream tube entering the propeller disc was accelerated inboard of the propeller tip, but the acceleration died out at the tip as expected. The peak velocity defect was approximately 0.15 at the 305 mm station, and had a wake width of about 15 mm measured midway between the minimum and maximum values of $\bar{U}$.

Y-Tail

Velocity data presented in the following section are referenced to the Y-tail trailing edge. The two upper surfaces of the Y-tail were installed with a positive dihedral of 34° as shown in figure 3(b). Survey traverses of this configuration were obtained along a vertical line and corrected to correspond to surveys perpendicular to the aerodynamic surface (fig. 10).

Mean velocity surveys of the Y-tail with the propeller operating are presented in figures 15 and 16 for Z locations of 178 and 262 mm, respectively. Those vertical surveys crossed the Y-tail wake 215 mm and 316 mm, respectively, from the fuselage centerline as measured radially. The propeller tip was 295 mm from the centerline. The magnitude and location of the wake are similar for the two cases; however, acceleration effects seen at 262 mm are absent at 178 mm.

Wake Growth

Figure 17 shows the maximum wake deficit, $\bar{U}_{max}$, plotted versus streamwise distance from the empennage for several empennage/survey conditions. The values of $\bar{U}_{max}$ were read from figures 12 through 15. The curves show a rapid decrease in wake deficit out to 100 mm and a gradual decay thereafter. That distance is equal to around 20 to 30% of the empennage chord. Propeller operation caused no significant change in peak deficit in the wake. It is clear, however, that of the two empennages tested, the Y-tail generated the smaller wake deficit because of its smaller chord and thickness.

Figure 18 shows the empennage wake widths plotted versus streamwise distance for the same data sets used in figure 17. The wake widths were measured midway between the minimum and maximum value of $\bar{U}$. The wakes were 6 to 10 mm wide near the empennage, and spread to a width of 15 to 20 mm at the farthest survey stations, $X' = 320$ mm and 470 mm. There is some scatter in the data, but the values fell

within a band 5 mm wide. The wake widths spread at an average rate of around 0.03 mm per mm of distance downstream. Although there is an indication that propeller operation narrowed the wakes slightly, any consistent trend was masked by the data scatter.

The empennage wake development can be compared with the theoretical analyses of wakes behind cylinders and flat plates. Schlichting (ref. 8) showed that the maximum wake deficit in a self-preserving, two-dimensional wake behind a cylinder is proportional to the square root of the product of the diameter and drag coefficient, and inversely proportional to the square root of the streamwise distance from the cylinder.

$$\bar{U}_{max} \propto \left(\frac{dC_d}{X'}\right)^{1/2} \tag{2}$$

The question remains, is the wake behind a cylinder analogous to the wake behind an airfoil? Chevray and Kovasznay (ref. 9) showed that the wake deficit behind a flat plate with zero streamwise pressure gradient is proportional to the square root of the boundary-layer momentum thickness ϕ and inversely proportional to the square root of the streamwise distance. Thus,

$$\bar{U}_{max} \propto \left(\frac{\phi}{X'}\right)^{1/2} \tag{3}$$

Furthermore, from Schlichting (ref. 8), the momentum thickness on a flat plate is related to the chord and drag coefficient as follows.

$$\phi \propto \left(\frac{cC_d}{2}\right) \tag{4}$$

Therefore, combining equations 3 and 4, we see that the wake deficit behind a flat plate is

$$\bar{U}_{max} \propto \left(\frac{cC_d}{2X'}\right)^{1/2} \tag{5}$$

which is similar to the wake deficit of a cylinder given by equation 2 if the diameter is replaced by the half chord. Since an airfoil, as a wake generator, is somewhere between a cylinder and a flat plate, it can be assumed that equation 5 is also valid for the empennages used in this study. Inverting the equation, we obtain

$$\bar{U}_{max}^{-2} \propto \left(\frac{2X'}{cC_d}\right) \tag{6}$$

Figure 19 shows plots of the inverse square of the peak velocity deficit, $\bar{U}_{max}^{-2}$, versus streamwise distance, X′, for the vertical tail fin and Y-tail. Data are presented for specific survey locations with and without the propeller operating. The curves are linear, as predicted by equation 6. Also, the Y-tail values of $\bar{U}_{max}^{-2}$ are greater than those of the vertical tail fin since the Y-tail chord was less than the vertical tail-fin chord. Similarly, the surveys of the vertical tail fin at Y = 305 mm show higher values of $\bar{U}_{max}^{-2}$ than at Y = 203 mm because the empennage chord is less at Y = 305 mm than at Y = 203 mm. No attempt was made to evaluate the implied proportionality constants in equations 2 through 6. These results indicate that classical models for wake growth can be used for empennage wakes of the type generated in this study, and the models do not have to be modified to account for propeller operation as studied here.

Flow Angle

The effect of propeller rotation on stream angle was observed in traverses of the vertical tail-fin wake with the directional pressure probe. Figures 20(a) and (b) show the measured yaw and pitch angles (β and θ) at Y = 210 mm, with propeller off. Figures 20(c) and (d) show the same type of data with 8200 propeller rpm. The measured yaw angles were small. There was some indication of flow moving toward the survey rig (positive β) in the region between the empennage and flow rig (positive Z) which could be caused by flow accelerations between the survey rig and empennage (see discussion of fig. 11). The data revealed no distinctive changes in measured-flow yaw angle, β, caused by propeller rotation. The pitch angle, θ, showed negative values (upwash) with the propeller removed (fig. 20(b)). This is expected in this region, which is upstream of the propeller motor mount, because of flow blockage by the motor nacelle and strut. The pitch angle reduced to nearly zero near the propeller with the propeller operating (fig. 20(d), X′= 369 mm), presumably because the flow acceleration into the propeller disc overcame the upwash.

Similar stream-angle data measured at Y = 305 and 311 mm (approximate propeller tip height) are shown in figures 21(a) through (d), and have similar trends as measured at Y = 210 mm (figs. 20(a) through (d)). In the present empennage configurations, which had spans longer than the propeller radius, any minor variations of stream angle caused by the empennage would probably not affect acoustic radiation. If the empennage had a span smaller than the propeller radius, however, the flow angularity induced by a tip vortex, for example, could have a substantial effect on propeller loading and noise.

Turbulent Velocity Effects

Propeller acoustic radiation consists of harmonically related tones and broadband noise. The harmonic components can be related to propeller interactions with the steady (uniform and nonuniform) inflow-velocity field. The turbulent velocity field, which contributes to the broadband noise, also can affect the harmonic noise if the turbulent eddies have sufficient length scale and amplitude to induce periodic blade loading.

Typical hot-wire spectra (10 log (rms voltage^2)) from a single 45° wire are presented in figure 22. The spectra were generated with a constant-bandwidth analyzer set at a nominal 25-Hz filter width. The data were acquired near the propeller tip height (Y = 305 mm), inside and outside the vertical tail-fin wake at two streamwise locations. The propeller-on data were acquired 106 mm upstream of the propeller tip, and the propeller-off data were acquired 274 mm upstream of the propeller station. Those two survey stations were 277 mm and 109 mm downstream of the vertical fin, propeller on and off, respectively. The spectra outside the wake (76 mm from the center of the wake) show strong periodic disturbances from the propeller. The peaks in the spectrum occur at multiples of the blade-passage frequency, which was 550 Hz (number of blades times revolutions per second). The hot-wire spectra in the wake are much more broadband, though the propeller disturbances are visible at the first two harmonics of the propeller blade-passage interactions. The peak in the wake spectrum at 1.53 kHz corresponds to a disturbance period, T, of 6.54 x10^{-4} sec/cycle (T = 1/f). If one assumes that that disturbance is related to a turbulent eddy traveling at a velocity equal to U in the center of the wake (40 m/sec), then the eddy length, l can be computed from:

$$l = U \times T = 40 \times 6.54 \times 10^{-4} = 0.0261 \text{ m or } 26 \text{ mm} \quad (7)$$

That dimension is approximately equal to the total wake width at that streamwise location.

As expected, the wake turbulence intensities are much stronger than those out of the wake, which is consistent with the plots of unfiltered hot-wire data shown in figure 23. The in-wake data (fig. 22), with propeller off, appear somewhat high because that data set had not yet decayed to the turbulence levels of the propeller-on curve acquired 168 mm farther downstream. Despite the strong propeller disturbances, the empennage wake turbulence upstream of the propeller was not amplified by the propeller.

Surveys of the vertical tail-fin streamwise wake-turbulence characteristics, u'/U_∞, are shown in figures 23(a) and (b) for propeller off and propeller on (8200 rpm). Similarly, the transverse components, v'/U_∞ and w'/U_∞ (propeller off and on), are presented in figures 24(a) and (b) and 25(a) and (b), respectively. These Z traverses were made at a vertical location of 305 mm and at four X′ locations. Since this Y station is comparable to the propeller radius, acceleration effects are minimal. The turbulence for the two cases (propeller on and off) are similar. The maximum u'/U_∞ and v'/U_∞ components are nearly equal throughout the wake region and varied from approximately 0.04 at X′ = 44 mm to 0.025 at X′ = 310 mm. The w'/U_∞ component (maximum intensity) was slightly larger than the other components, with a variation with distance from approximately 0.05 at X′= 31 mm to 0.03 at 301 mm.

Figure 26 shows vertical surveys of u'/U_∞ in the wake of the Y-tail, 160 mm to the side of the centerline. The width and intensity of the turbulent wake is similar to the cases previously described, except that the base turbulence level decreases from approximately 0.055 near the tail (X′= 63 mm) to 0.025 near the propeller (X′ = 510 mm). This last station is only 63 mm upstream of the propeller. The increase in turbulence outside of the wake at X′= 510 mm is attributable to the unsteady velocity field associated with the propeller.

CONCLUDING REMARKS

This paper describes a flow survey in the Ames 7- by 10- Foot Wind Tunnel of the velocity field between two empennage models and a pusher propeller. The study sought to document the flow field experienced by the propeller and to determine the effects of propeller rotation on wake modification or displacement. Observation of the wake mean-velocity defect and spreading were consistent with analytical predictions of wakes from two-dimensional bodies. The mean velocity deficit in the wake decayed rapidly from the empennage trailing edge to a distance equal to approximately 0.2 to 0.3 empennage chords, and decayed less rapidly thereafter. At the propeller station, less than one propeller diameter behind the empennage, the normalized wake deficit was typically 0.10 to 0.15.

Although propeller pressure disturbances were visible in the hot-wire signals in the wake, the effect of propeller rotation on the wake turbulence was small. The peak turbulence in the wake near the propeller tip was around 3 % of the free-stream velocity.

In general, no strong effects of wake intensification (velocity defect increase) or broadening by the propeller were observed, although the propeller did accelerate the flow at its midspan. In general, the results suggest that models of the wake for acoustic prediction may neglect the effect of propeller rotation for the range of parameters of this study. It would be desirable to expand the scope of this study in the future to include the effects of empennage control-surface deflection.

APPENDIX

HOT-WIRE ANEMOMETER DATA REDUCTION ALGORITHMS

Probe Designation	Type	Wire Designation	Anemometer Output	Amplifier Output
Probe A	55P63	Wire #1	E_1	V_1
	(u-w)	Wire #2	E_2	V_2
Probe B	55P64	Wire #3	E_3	V_3
	(u-v)	Wire #4	E_4	V_4

(see fig. 7 for hardware layout)

Summary of Measurement and Data Reduction Procedure

A) Calibration

1. Move probe into undisturbed uniform air stream. Set probe to zero yaw angle (β).

2. Record V_I (for wires I =1,2,3,4) versus U_∞ for approximately 10 settings of wind tunnel airspeed (measured with a pitot-static probe). The amplified anemometer voltages are used nonlinearized.

3. Calculate best line fit for

$$E_I^2 = C_I + D_I (U_\infty)^{1/2}$$

where $E_I = (V_I - A_I)/B_I$

A_I = amplifier offset voltage
B_I = amplifier gain
C_I, D_I are constants for least-square fit to above equation

The hot wire can now be used to measure velocity for zero probe angle; i.e.,

$$U_\infty = \left[\frac{E_I^2 - C_I}{D_I}\right]^2$$

If the yaw angle, β, is not zero, the anemometer voltage corresponds to a velocity, U_{eff_I}, which is the effective velocity parallel to the probe axis that would give the same voltage as measured by the hot wire I.

$$U_{eff_I} = \left[\frac{E_I^2 - C_I}{D_I}\right]^2$$

The velocity U_{eff_I} is a function of probe yaw angle, β, wire angle, α, and U_∞. (The wire angle enters only if the wire is repaired or replaced.)

B) Measurements to acquire turbulence components

1. Traverse probe to desired location.
2. Acquire N successive simultaneous samples of E_1, E_2, E_3, E_4; N > 1000.
3. Decompose hot wire signal.

$$E_I = \bar{E}_I + E_I'$$

$\bar{E}_I$ = average of E_I

E_I' = unsteady component of E_I

4. Compute and store.

$E_1, E_2, E_3, E_4,$

$\overline{(E_1')^2}, \overline{(E_2')^2}, \overline{(E_3')^2}, \overline{(E_4')^2},$

$\overline{(E_1')^2(E_2')^2}, \overline{(E_3')^2(E_4')^2},$

C) Reduction

1. Compute the mean effective velocity quantities.

a) $U_{eff_I} \cong 0.721 \left[\left(\bar{E}_I^2 - C_I \right)^2 + \left(6\bar{E}_I^2 - 2\,C_I \right) \overline{(E_I'^2)} \right] / D_I^2$ where I = 1,2,3,4

b) $\overline{(U'eff_I)^2} \cong 8.32 \left[\left(\bar{E}_I^3 - \bar{E}_I C_I \right)^2 \overline{(E_I')^2} \right] / D_I^4$ where I = 1,2,3,4

c) $\overline{(U'eff_I)(U'eff_J)} \cong 8.32 \left[\left(\bar{E}_I^3 - \bar{E}_I C_I \right) \left(\bar{E}_J^3 - C_J \bar{E}_J \right) \overline{(E_I')(E_J')} \right] / D_I^2 D_J^2$ where I,J = 1,2,3,4

2) Compute mean and turbulent velocity quantities relative to the probe axis.

a)

$$\bar{u} \cong 0.693 \left(\bar{U}_{eff_1} + \bar{U}_{eff_2} \right) \cong 0.693 \left(\bar{U}_{eff_3} + \bar{U}_{eff_4} \right)$$

b)

$$\overline{w} \cong 0.751\left(\overline{U}_{eff_2} - \overline{U}_{eff_1}\right)$$

c)

$$\overline{v} \cong 0.751\left(\overline{U}_{eff_3} - \overline{U}_{eff_4}\right)$$

d)

$$\left[\overline{(u')^2}\right]^{0.5} \cong 0.693\left[\overline{\left(U'_{eff_1}\right)^2} + 2\,\overline{\left(U'_{eff_1}\right)\left(U'_{eff_2}\right)} + \overline{\left(U'_{eff_2}\right)^2}\right]^{0.5}$$

$$\cong 0.693\left[\overline{\left(U'_{eff_3}\right)^2} + 2\,\overline{\left(U'_{eff_3}\right)\left(U'_{eff_4}\right)} + \overline{\left(U'_{eff_4}\right)^2}\right]^{0.5}$$

$$\left[\overline{(v')^2}\right]^{0.5} \cong 0.751\left[\overline{\left(U'_{eff_2}\right)^2} - 2\,\overline{\left(U'_{eff_2}\right)\left(U'_{eff_1}\right)} + \overline{\left(U'_{eff_1}\right)^2}\right]^{0.5}$$

$$\left[\overline{(w')^2}\right]^{0.5} \cong 0.751\left[\overline{\left(U'_{eff_3}\right)^2} - 2\,\overline{\left(U'_{eff_3}\right)\left(U'_{eff_4}\right)} + \overline{\left(U'_{eff_4}\right)^2}\right]^{0.5}$$

e)

$$\overline{u'v'} \cong 0.520\left[\overline{\left(U'_{eff_3}\right)^2} - \overline{\left(U'_{eff_4}\right)^2}\right]$$

f)

$$\overline{u'w'} \cong 0.520\left[\overline{\left(U'_{eff_2}\right)^2} - \overline{\left(U'_{eff_1}\right)^2}\right]$$

Revised Data Reduction Procedure

The procedure described above was based on two approximations. It was assumed that:

1. The wires were perfectly inclined 45° to the mean flow direction, and the hot-wire response was ideal. (End effects were neglected.)

2. The turbulence scale was small enough that fluctuating velocity products could be computed from fluctuating voltage products. This requires a locally linear relationship on the nonlinear curve of velocity versus hot wire voltage.

These approximations are eliminated in a revised procedure which has been used subsequent to the study reported here. The improvements include incorporation of yaw angle calibrations and averaging of the computed velocity samples as follows.

Angle Calibration (for each X-wire probe)

Assume $u = a_{11} U_{eff_1} + a_{12} U_{eff_2}$

$v = a_{21} U_{eff_1} + a_{22} U_{eff_2}$

for ideal wires: $a_{11} = 0.5$ $a_{12} = 0.5$

$a_{21} = -0.5$ $a_{22} = 0.5$

Determine a_{ij} by a linear fit to the equations

$$u / U_{eff_1} = a_{11} + \left(a_{12} U_{eff_2} / U_{eff_1} \right)$$

$$v / U_{eff_1} = a_{12} + \left(a_{22} U_{eff_2} / U_{eff_1} \right)$$

X-wire probes are typically calibrated every 5° betweeen ±40°.

Measurements

u,v are computed for each sample. Components

$\bar{u}$, $\bar{v}$, $\left(\overline{u'^2}\right)^{0.5}$, $\left(\overline{v'^2}\right)^{0.5}$, $\left(\overline{u'v'}\right)$ are then computed directly from the array of velocity samples.

$$\bar{u} \cong \frac{1}{N} \sum_{n=1}^{N} u(n) \qquad n = 1 \ldots N \quad N = 1024$$

This procedure can be extended to triple wire probes with a 3 x 3 calibration matrix.

REFERENCES

1. Wilby, J.F.; and Wilby, E.G.: Wind Tunnel Acoustic Study of a Propeller Installed behind an Airplane Empennage: Data Report. NASA CR-177335, Jan. 1985.

2. Block, P.J.W.: Noise Generated by a Propeller in a Wake. NASA TM-85794, May 1984.

3. Block, P.J.W.: Analysis of Noise Measured From a Propeller in a Wake. NASA TP-2358, Nov. 1984.

4. Block, P.J.W.: Noise Radiation Patterns of Counter-Rotation and Unsteadily Loaded Single-Rotation Propellers. J. Aircraft, vol. 22, no. 9, Sept. 1985, pp. 777-783.

5. Mitchell, G.A.; and Mikkelson, D.C.: Summary and Recent Results from the NASA Advanced High-Speed Propeller Research Program. NASA TM-82891, 1983.

6. Tanna, H.K.; Burrin, R.H.; and Plumblee, H.E.Jr.: Installation Effects on Propeller Noise. J. Aircraft, vol. 18, no. 4, Apr. 1981, pp. 303-309.

7. Herkes, W.: An Experimental Study of the Noise Generated by A Pusher Propeller Due to A Wake Entering the Propeller Disc. von Karmen Institute, AFOSR 79-0033, Nov. 1979. (ADA078437).

8. Schlichting, H. (J. Kestin, transl.): Boundary-Layer Theory. McGraw-Hill Book Co., 1968.

9. Chevray, R. and Kovasznay, L. G.: Turbulence Measurements in the Wake of a Thin Flat Plate. AIAA J., vol. 7, no. 8, Aug. 1969, pp. 1641-1643.

ORIGINAL PAGE IS
OF POOR QUALITY

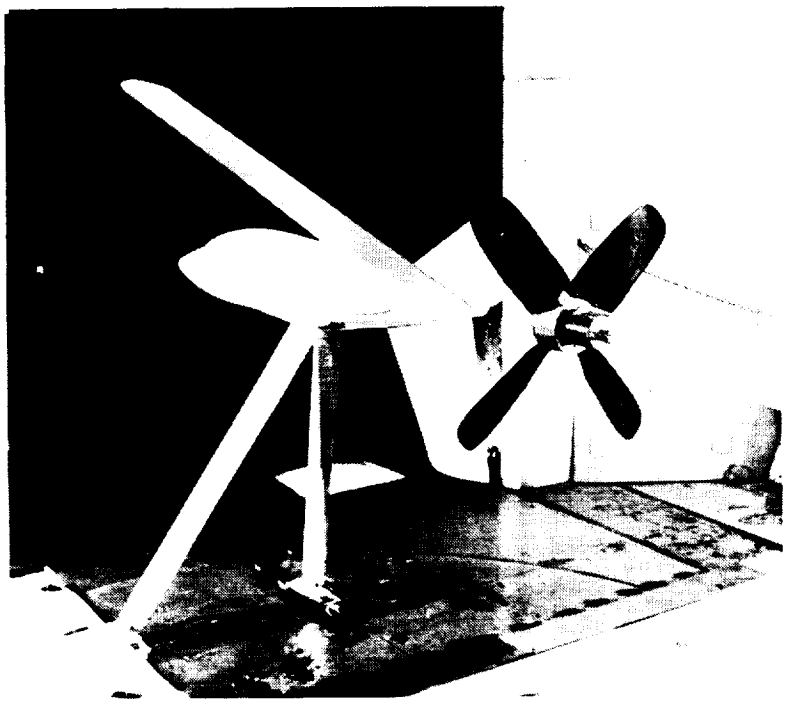

a) Y-tail

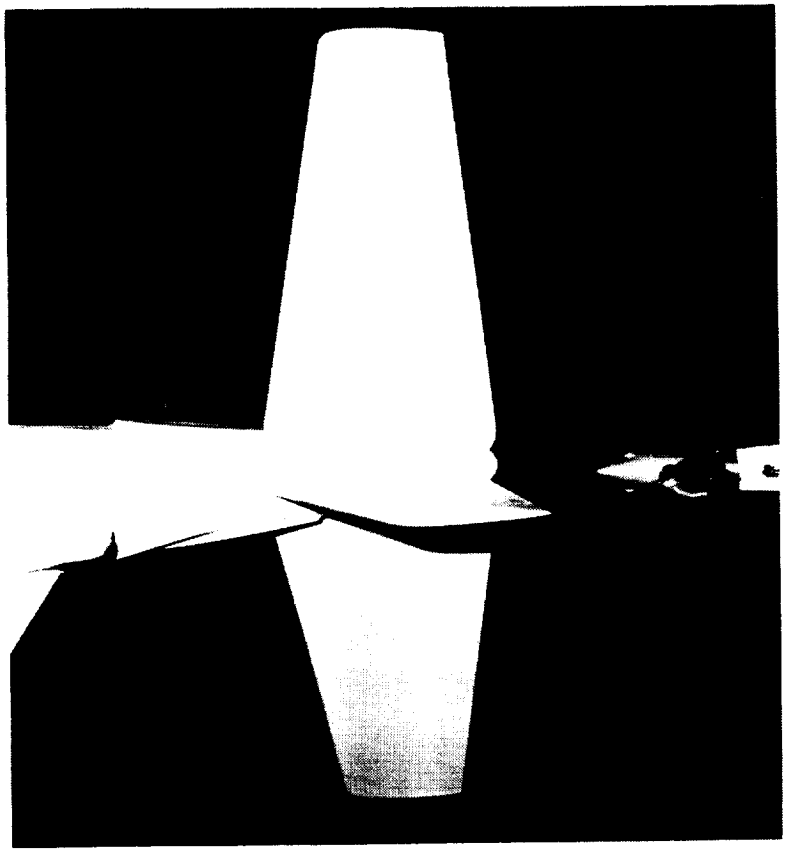

b) Y-tail empennage seen from below

Figure 1 – Photographs of model propeller, empennages, and fuselage in the Ames 7-by 10-Foot Wind Tunnel test section.

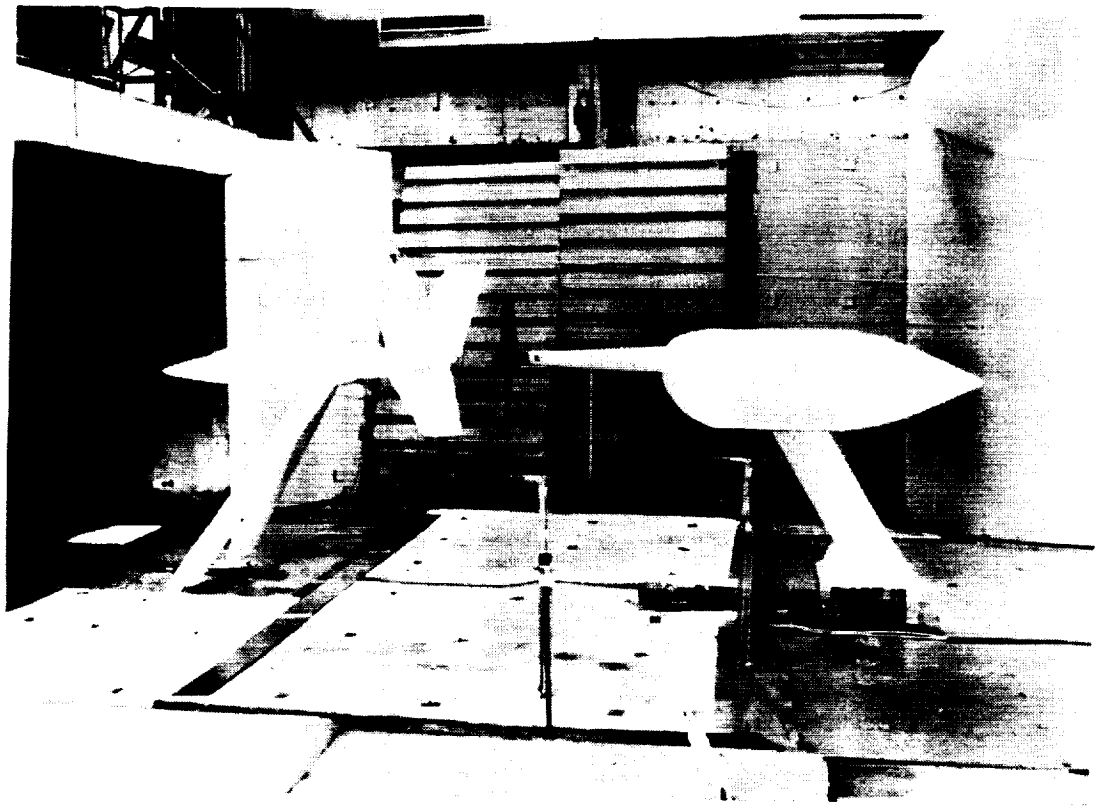

c) Open test section and Y-tail with sound-absorbing panels used to minimize reflections during acoustic tests.

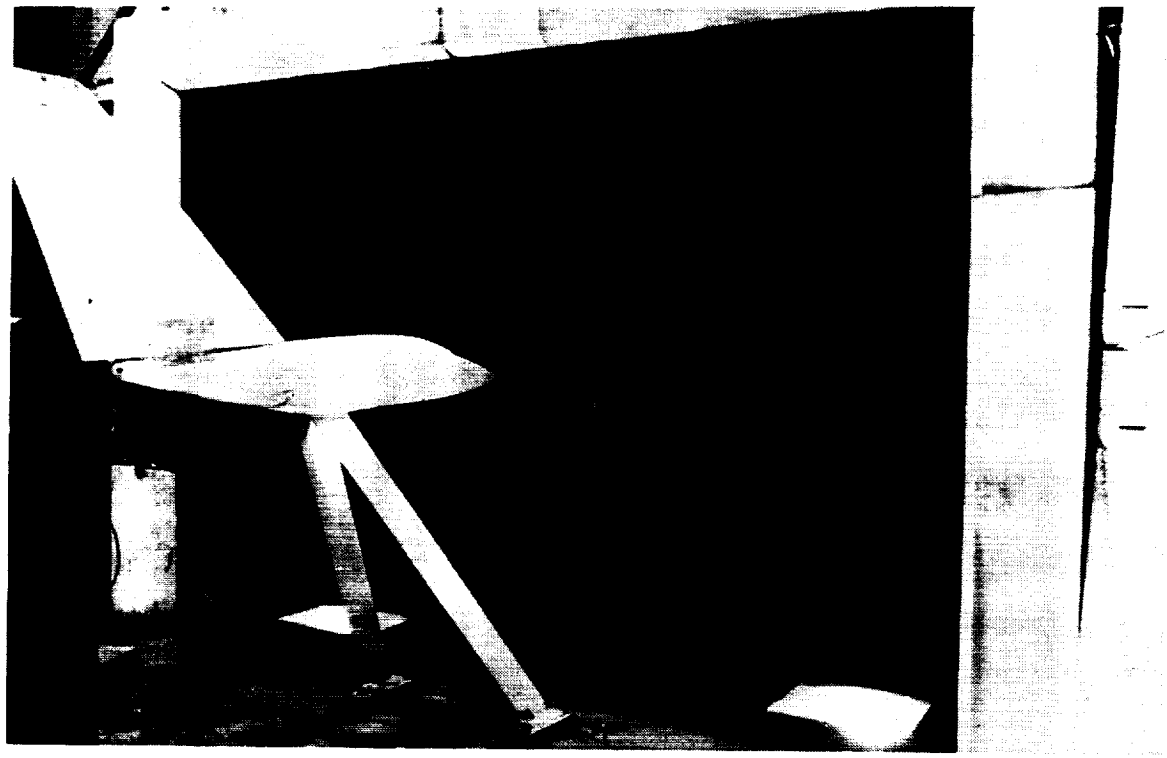

d) Vertical tail fin

Figure 1.– Concluded.

ORIGINAL PAGE IS
OF POOR QUALITY

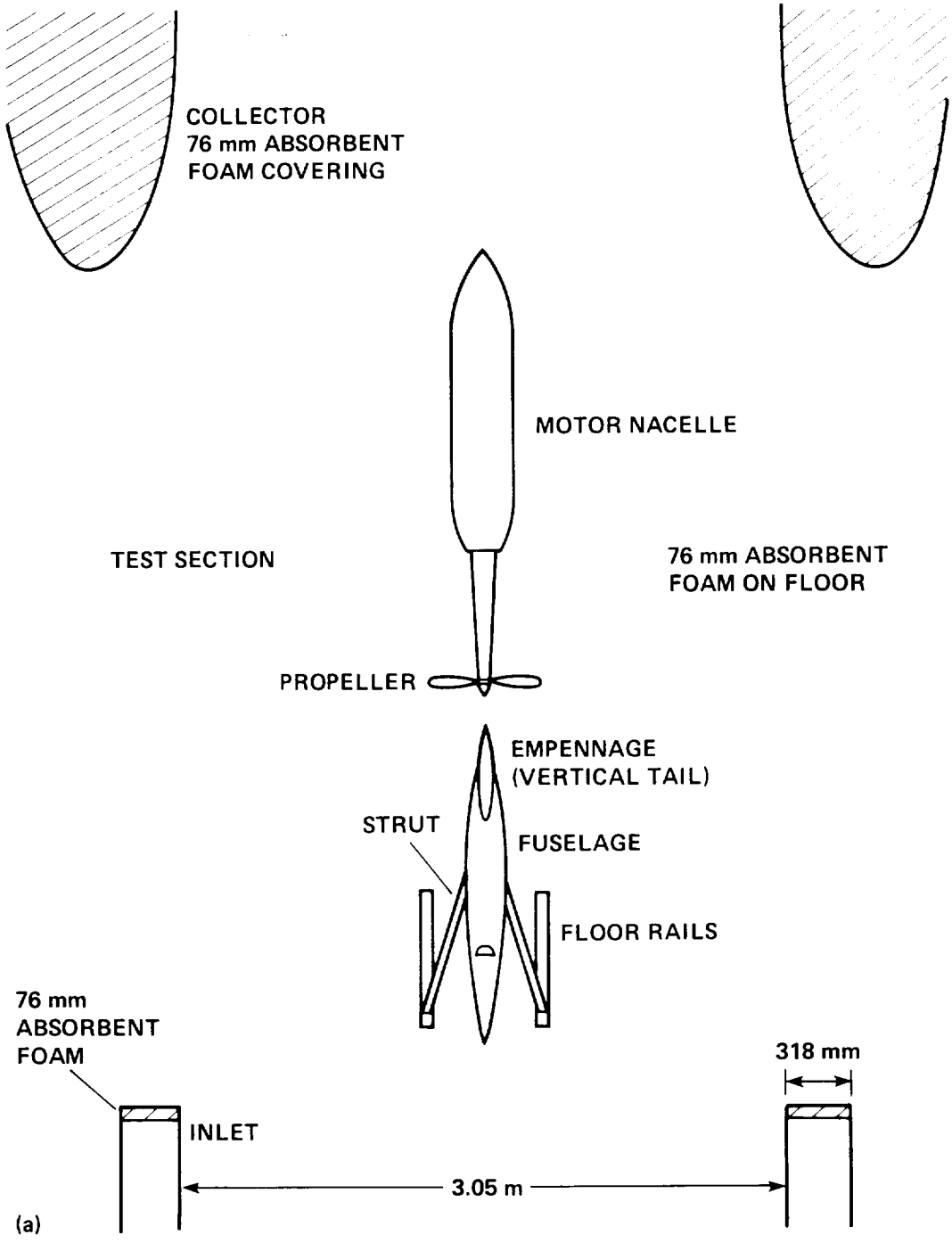

a) Plan view of test section

Figure 2.– Schematic of model in test section relative to inlet and collector.

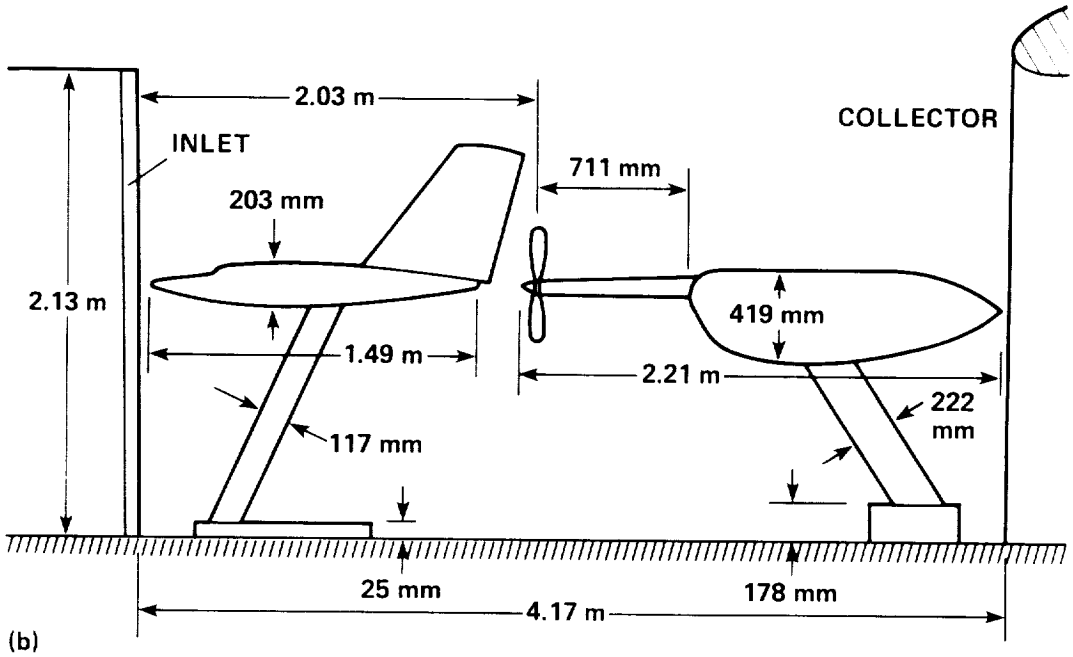

b) Elevation view

Figure 2.– Concluded.

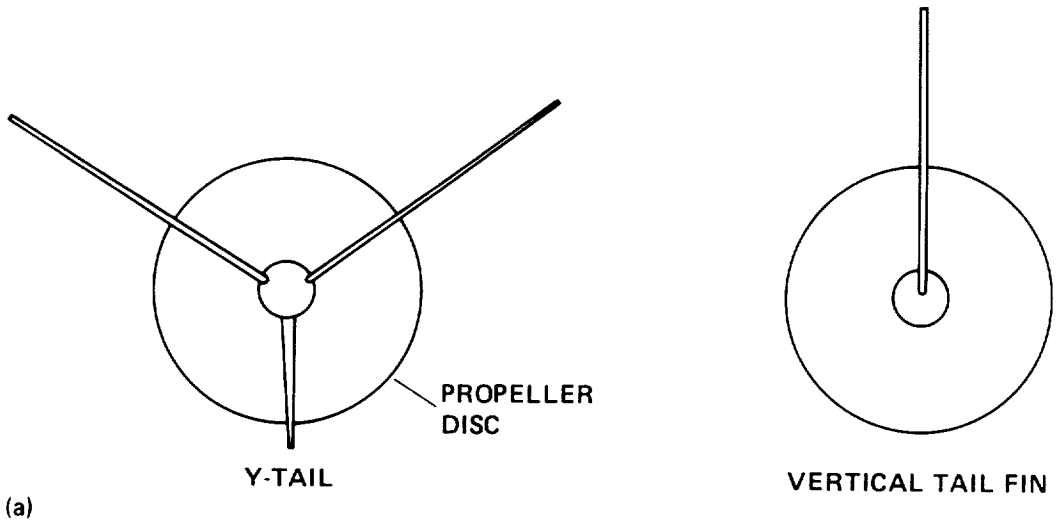

a) Looking downstream

Figure 3.– Geometry of empennages

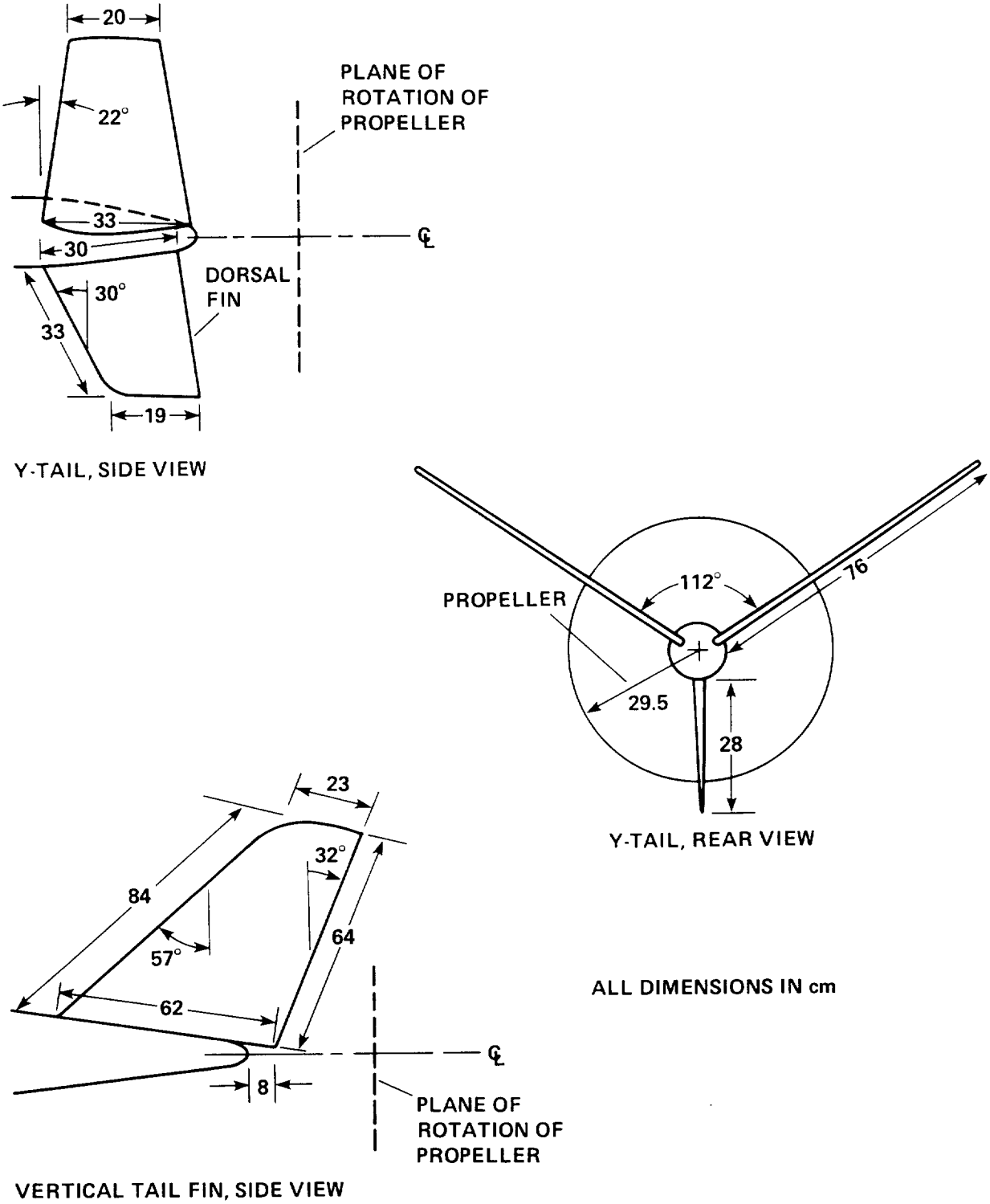

b) Dimensions

Figure 3.– Continued

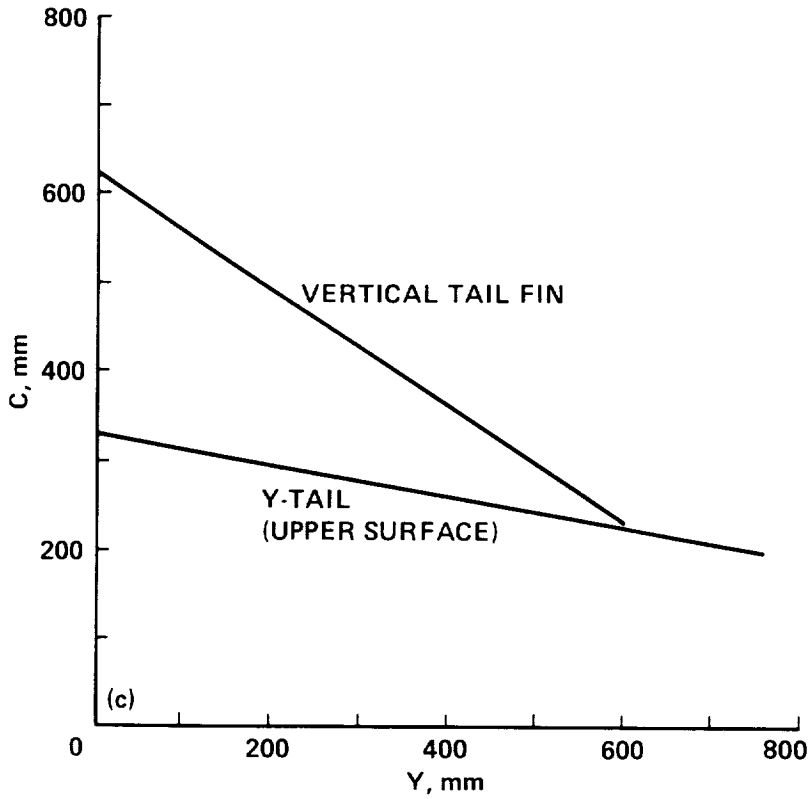

c) Chord distribution versus span station

Figure 3.– Concluded.

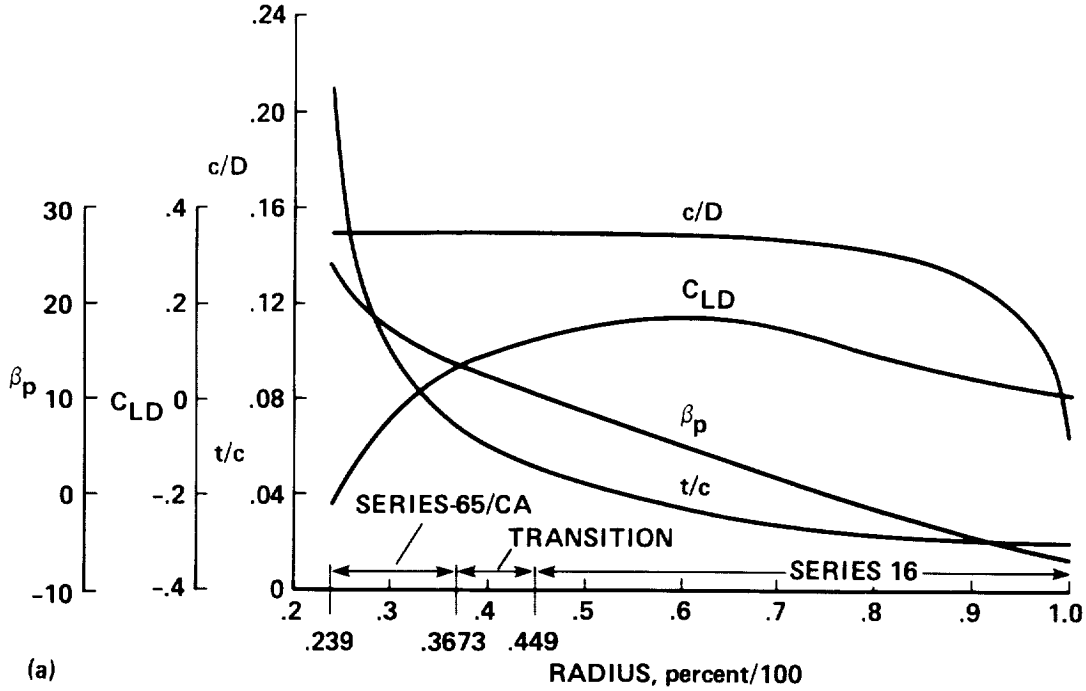

a) Radial distribution of chord (c), twist (β_p), thickness (t), and design lift coefficient (C_{LD}). The reference diameter (D) for this figure is 622 mm.

Figure 4.– SR-2 propeller geometry.

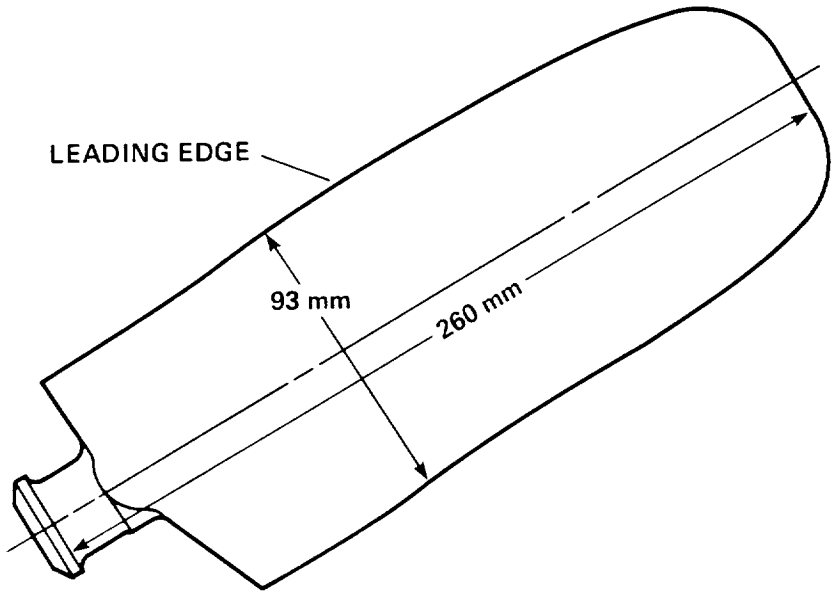

b) Blade planform

Figure 4.– Continued.

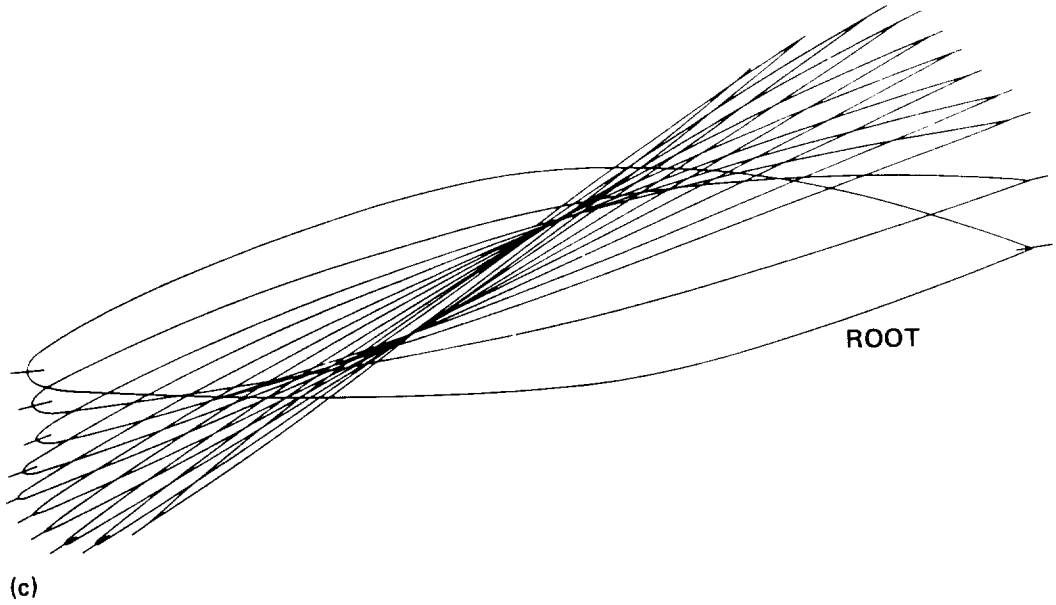

c) Blade airfoil sections at 12 radial stations from the root to tip

Figure 4.– Concluded.

ORIGINAL PAGE IS
OF POOR QUALITY

Figure 5.– Flow survey apparatus.

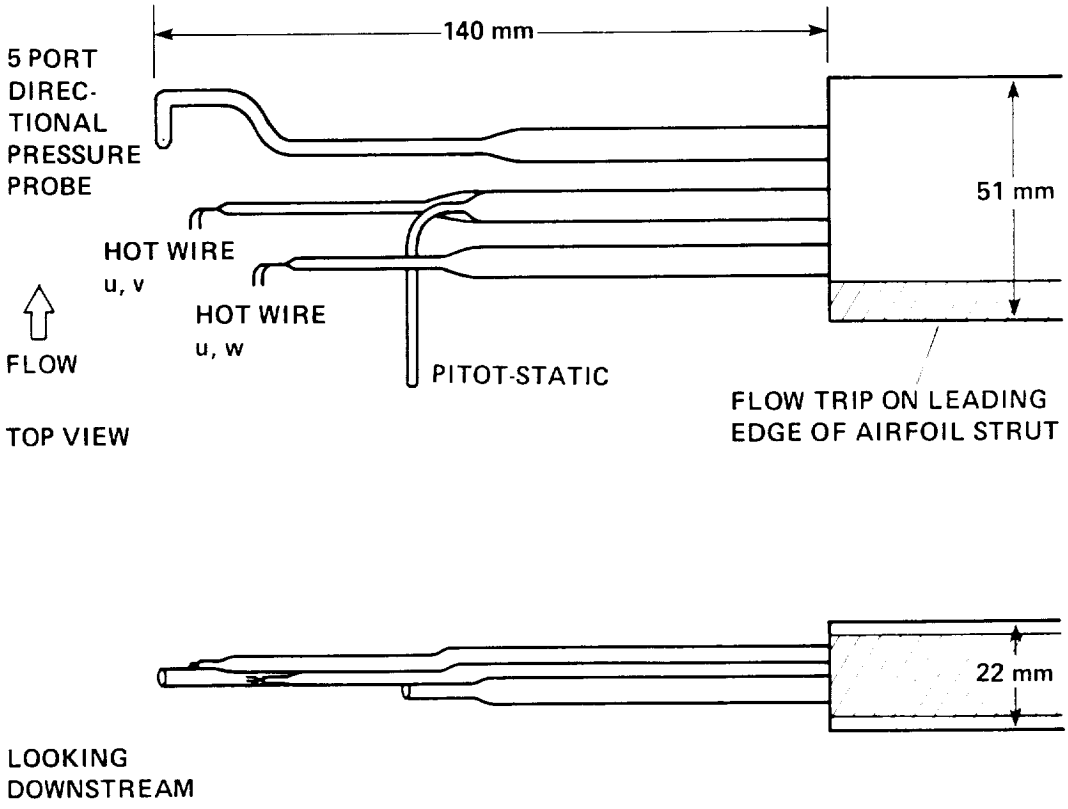

Figure 6.– Flow survey probes.

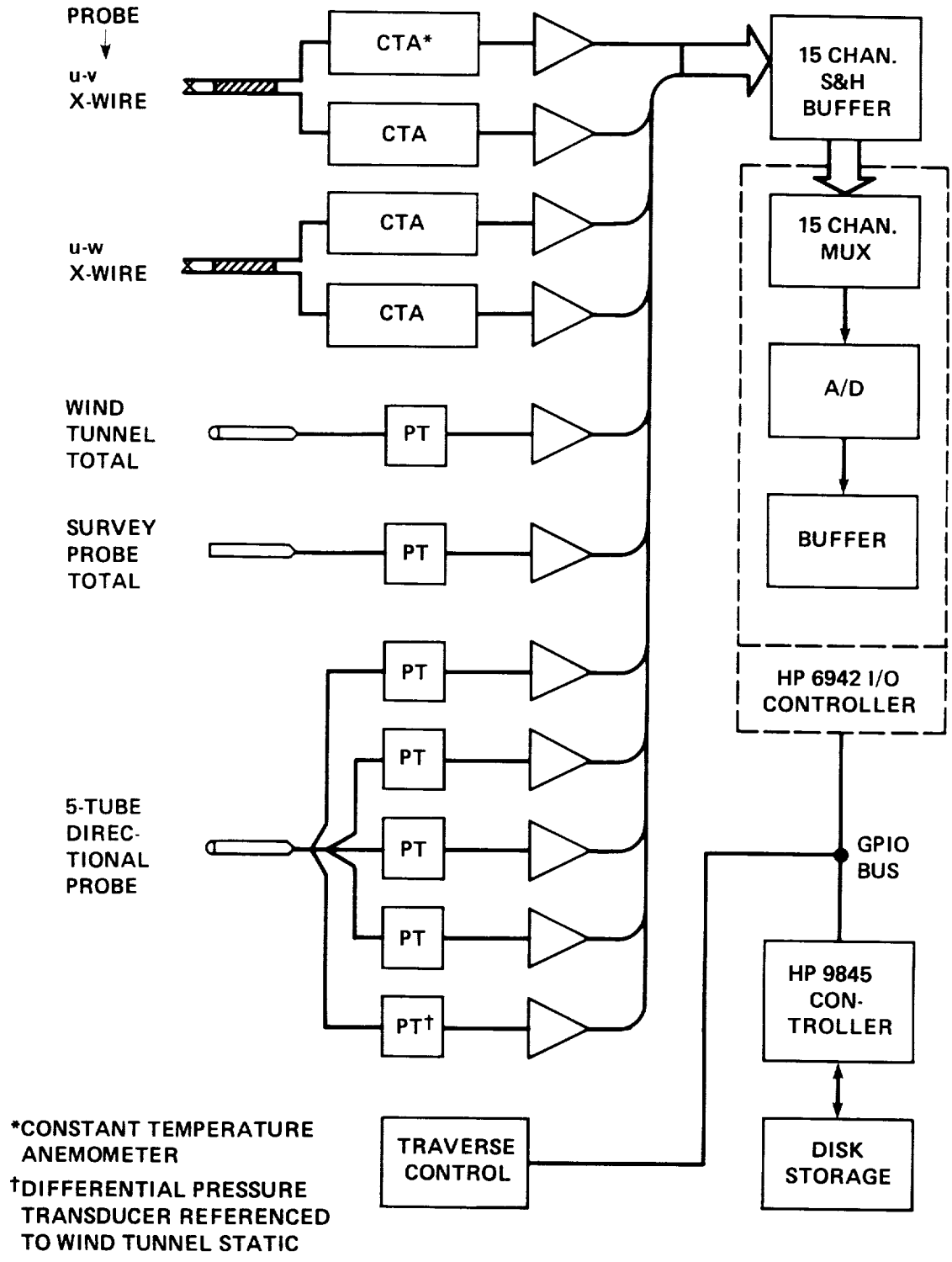

Figure 7.– Data acquisition system.

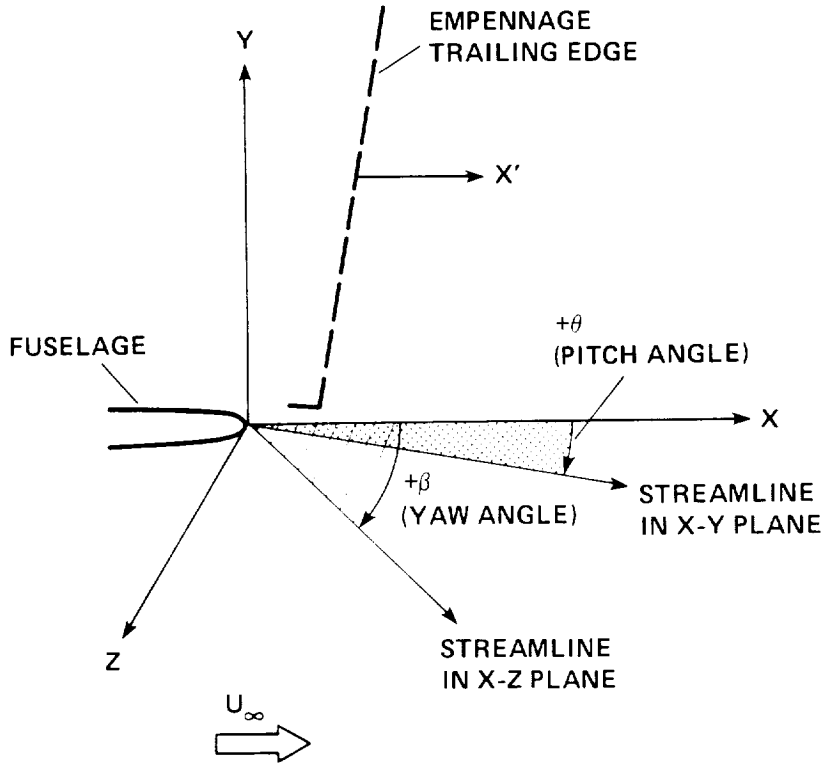

X, Y, Z FIXED COORDINATE SYSTEM WITH ORIGIN AT AFT TIP OF FUSELAGE

X' DISTANCE FROM A GIVEN POINT ON THE EMPENNAGE TRAILING EDGE IN THE x DIRECTION

Figure 8.– Coordinate system relative to fuselage tip (X,Y,Z) and relative to empennage trailing edge (X′). Flow angles ß and θ are shown.

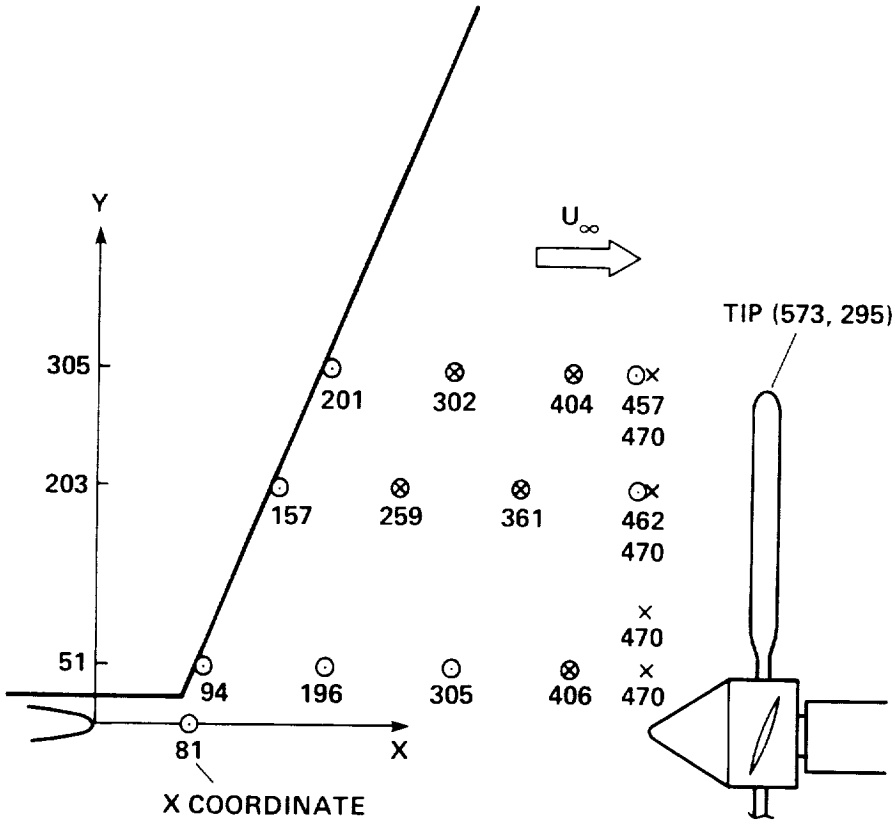

Figure 9.– Vertical tail fin survey locations in the X-Y plane. Traverses were in the Z direction.

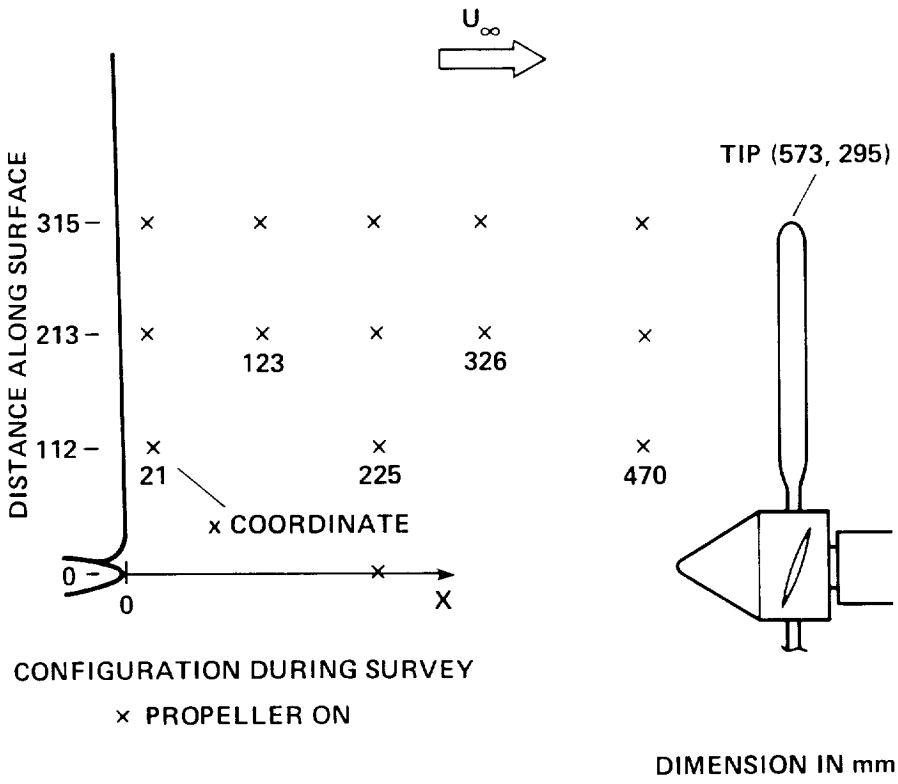

Figure 10.– View looking up at left surface of Y-tail showing locations where vertical survey traverses crossed wake center.

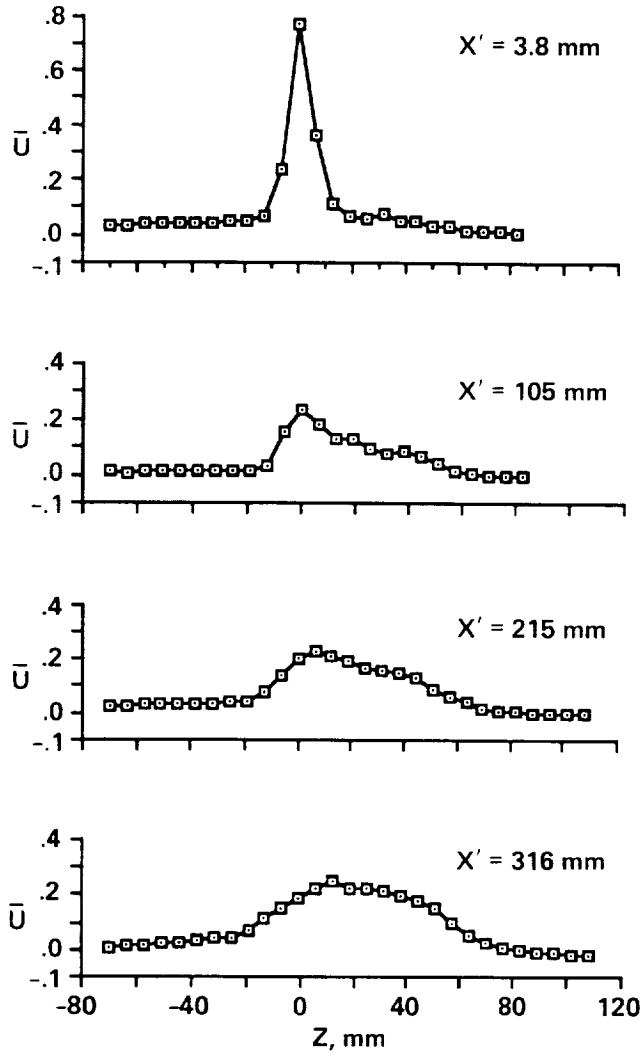

Figure 11.– Velocity deficit profiles measured at several streamwise locations behind the vertical tail fin - propeller off; Y = 51 mm.

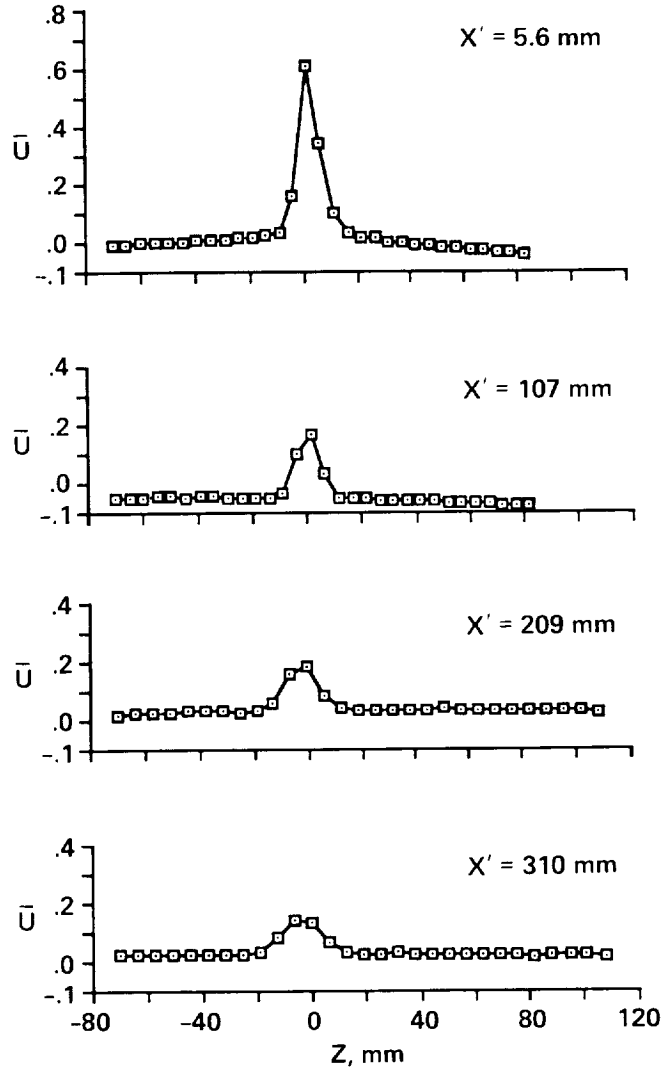

a) Propeller off

Figure 12.– Velocity deficit profiles behind the vertical tail fin - propeller off and propeller operating; Y = 203 mm.

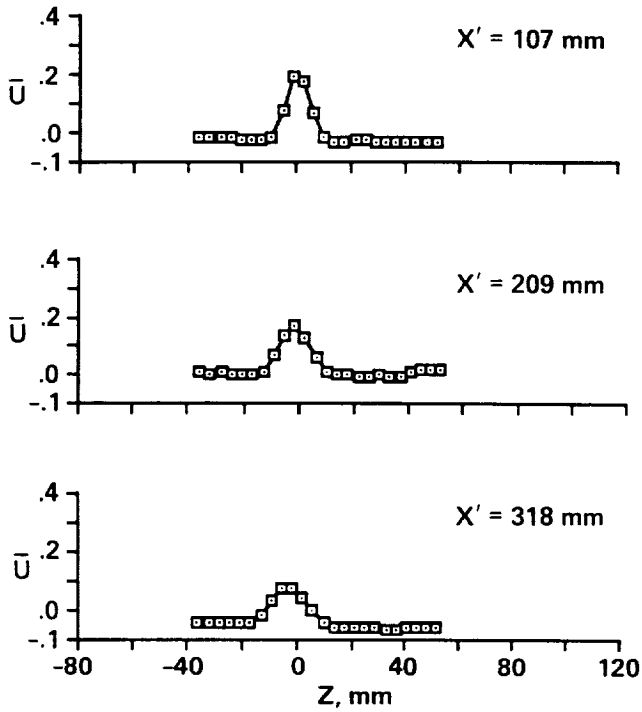

b) Propeller operating

Figure 12.– Continued.

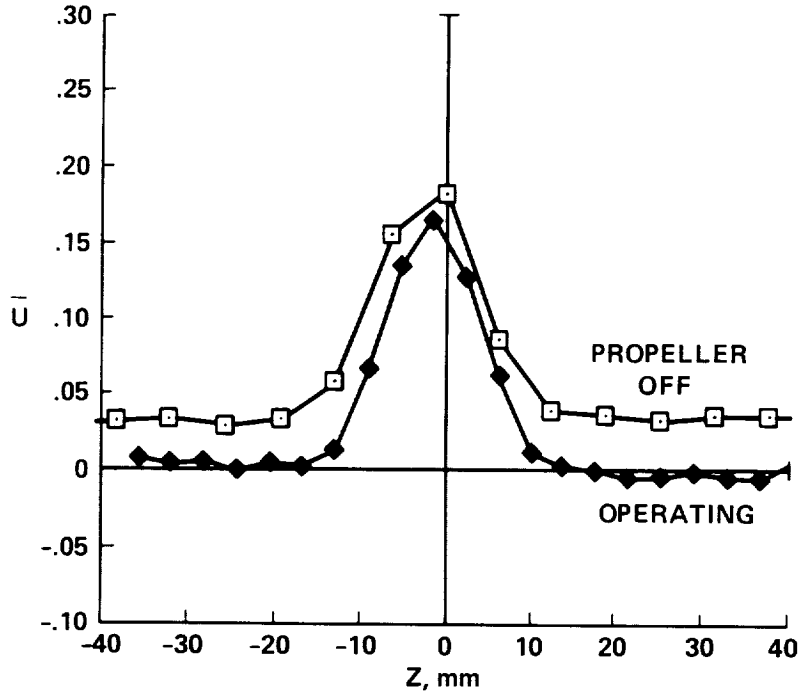

c) Propeller off and operating, X′= 209 mm

Figure 12.– Concluded.

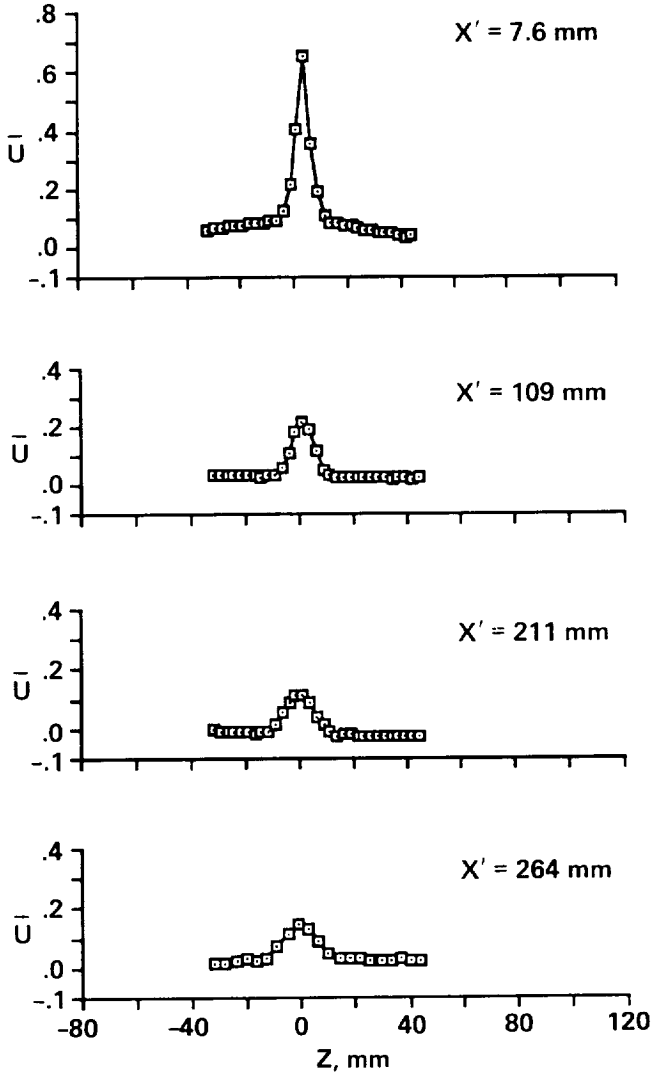

a) Propeller off

Figure 13.– Velocity deficit profiles behind the vertical tail fin - propeller off and propeller operating; Y = 305 mm.

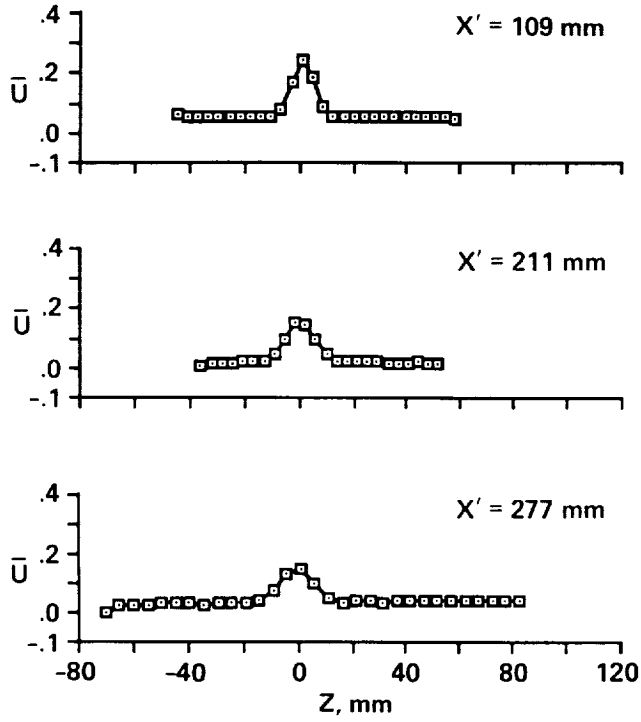

b) Propeller operating

Figure 13.– Concluded.

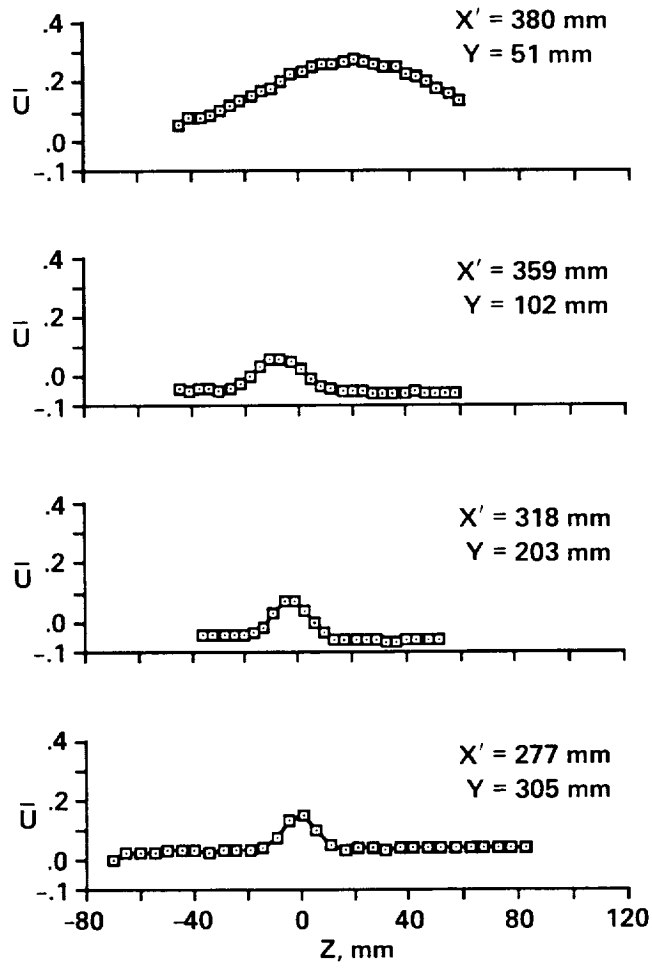

Figure 14.– Velocity deficit profiles at four vertical stations behind the vertical tail fin - propeller operating. Note that all surveys were made 103 mm upstream of the propeller. X' varies because of the sweep angle of the tail fin trailing edge.

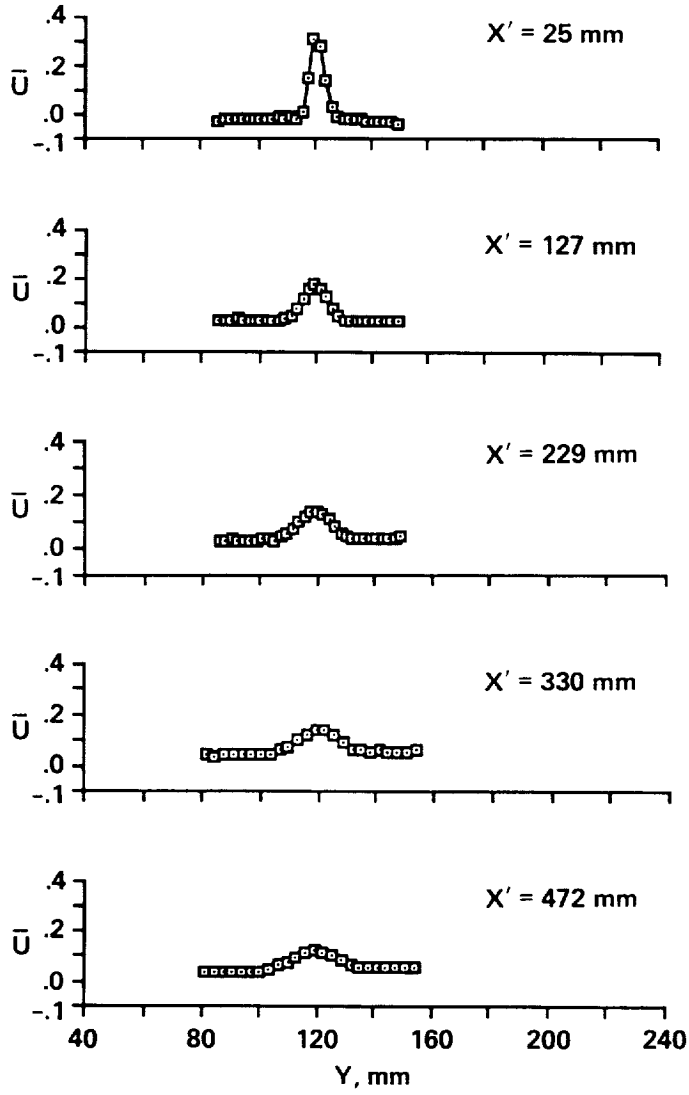

Figure 15.– Velocity deficit profiles behind the Y-tail with propeller operating; Z = 178 mm.

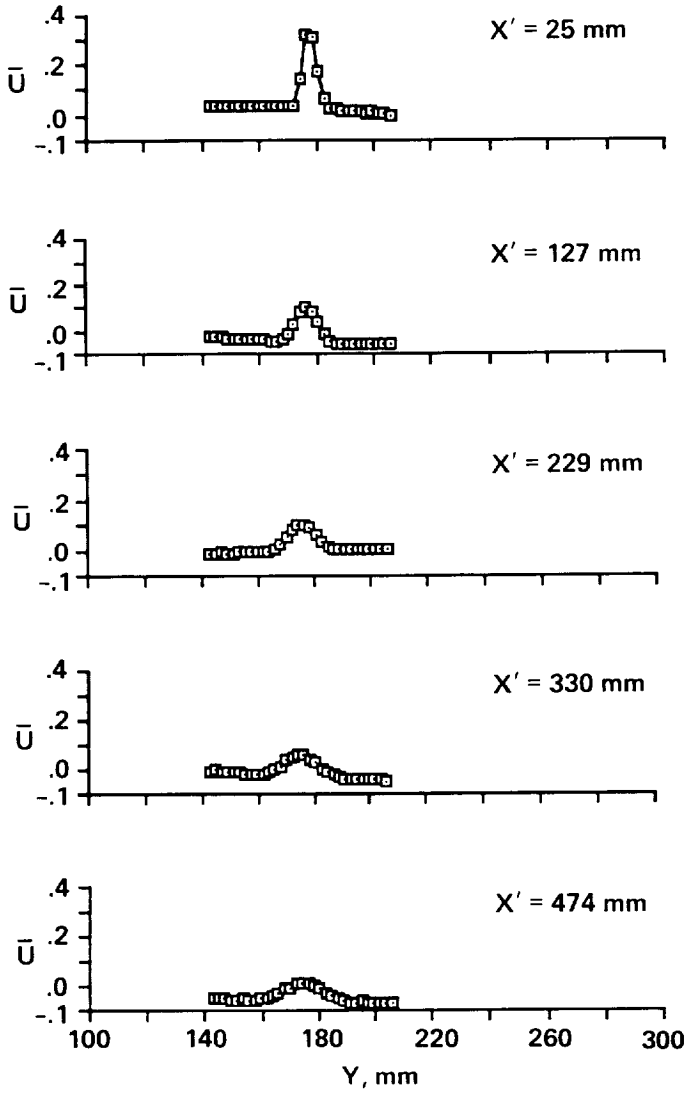

Figure 16.– Velocity deficit profiles behind the Y-tail with propeller operating; Z = 262 mm.

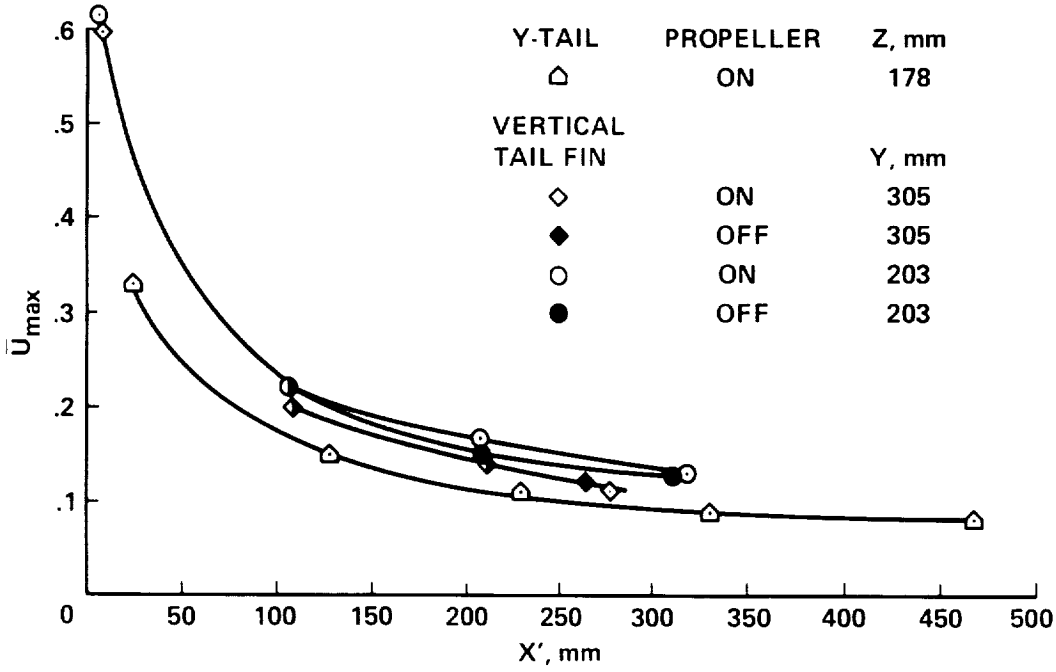

Figure 17.– Peak wake deficit versus distance from the empennage.

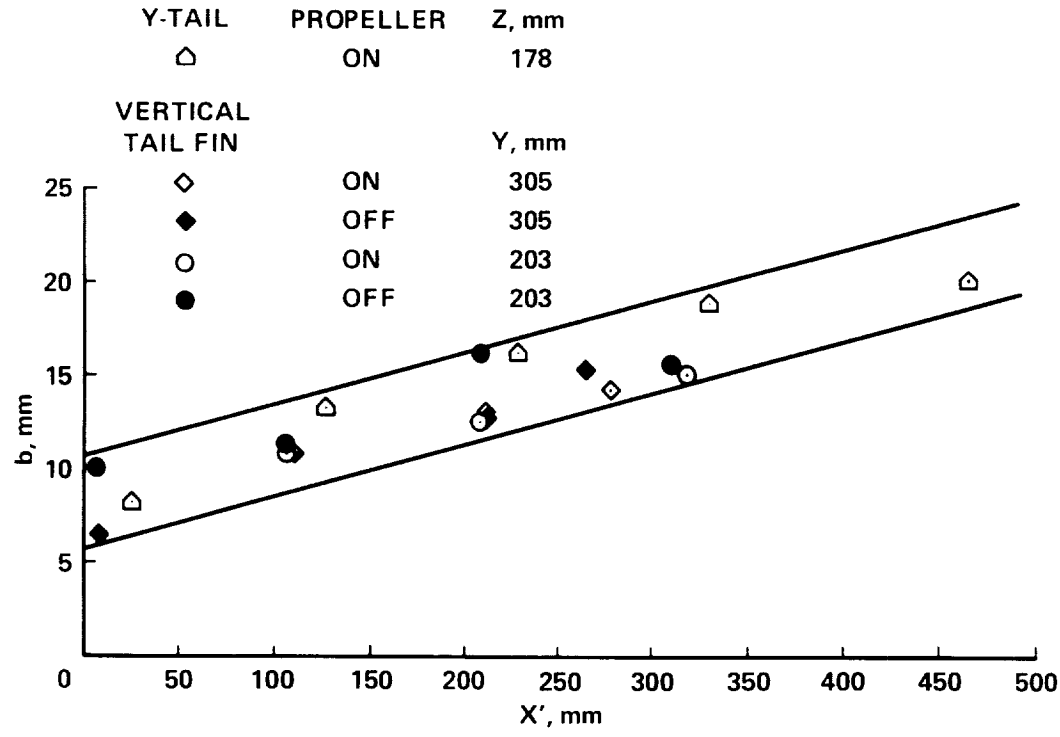

Figure 18.– Wake width at mid height of $\bar{U}_{max}$ versus distance from the empennage.

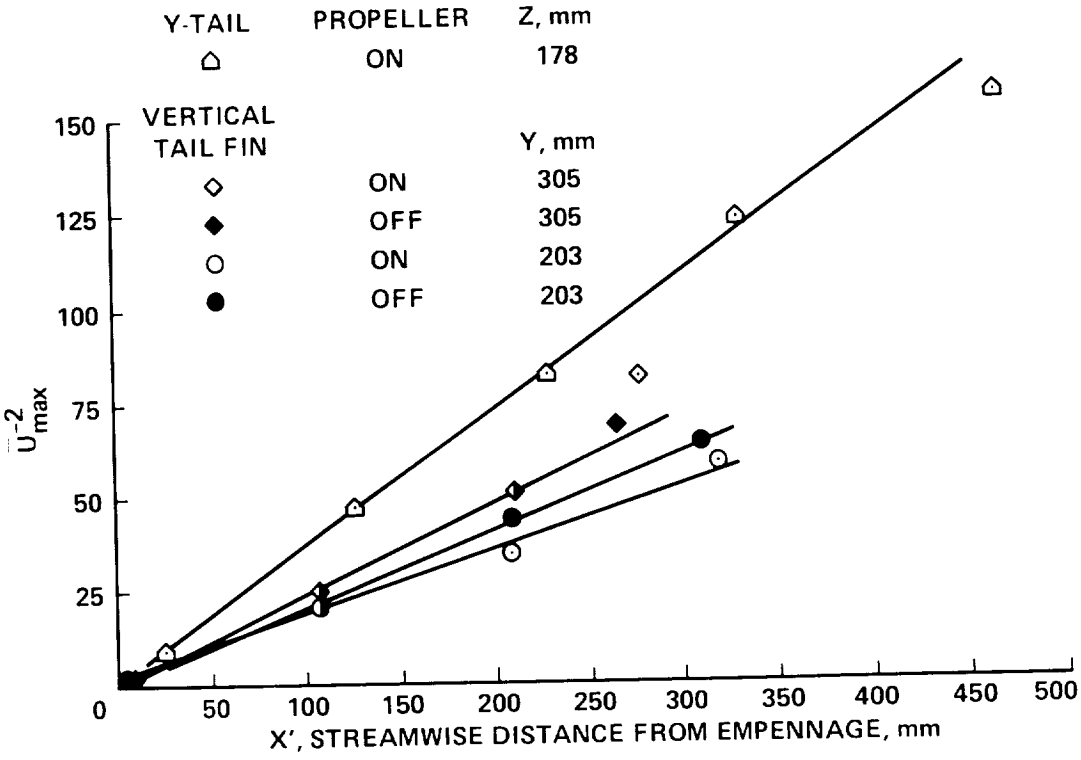

Figure 19.– Inverse square of peak velocity deficit versus streamwise distance from empennages.

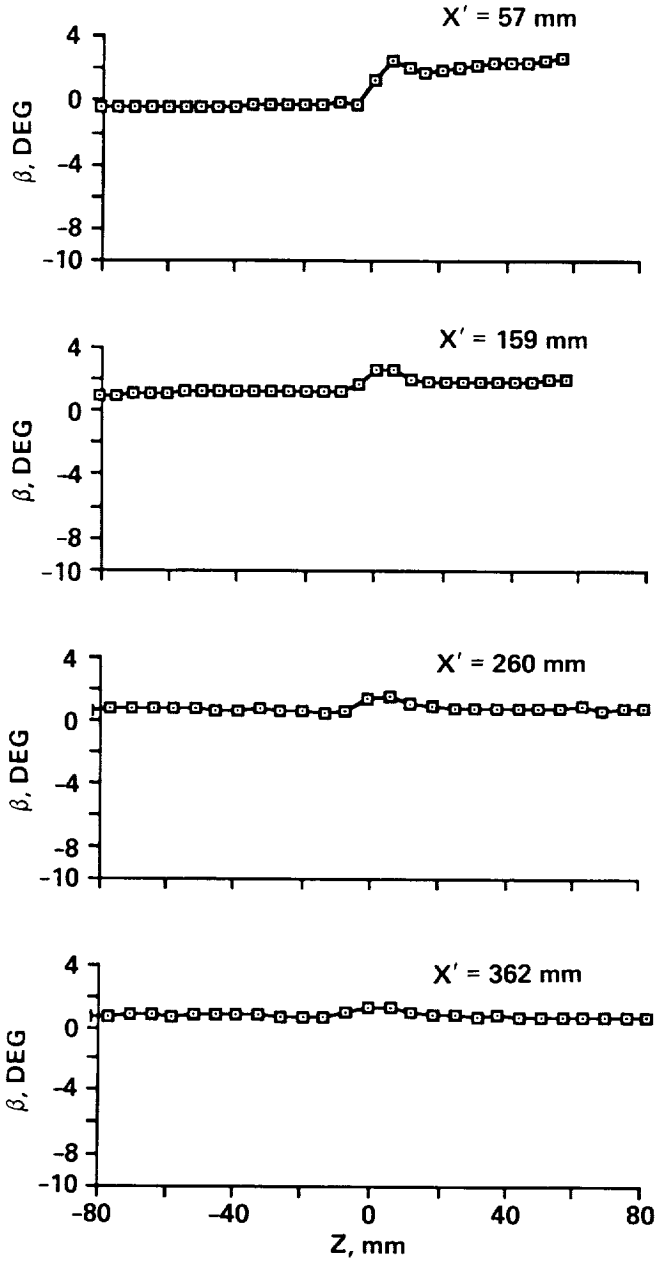

a) Yaw angle, ß, propeller off

Figure 20.– Flow yaw and pitch angle distributions through the vertical tail fin wake - propeller off and propeller operating; Y = 210 mm.

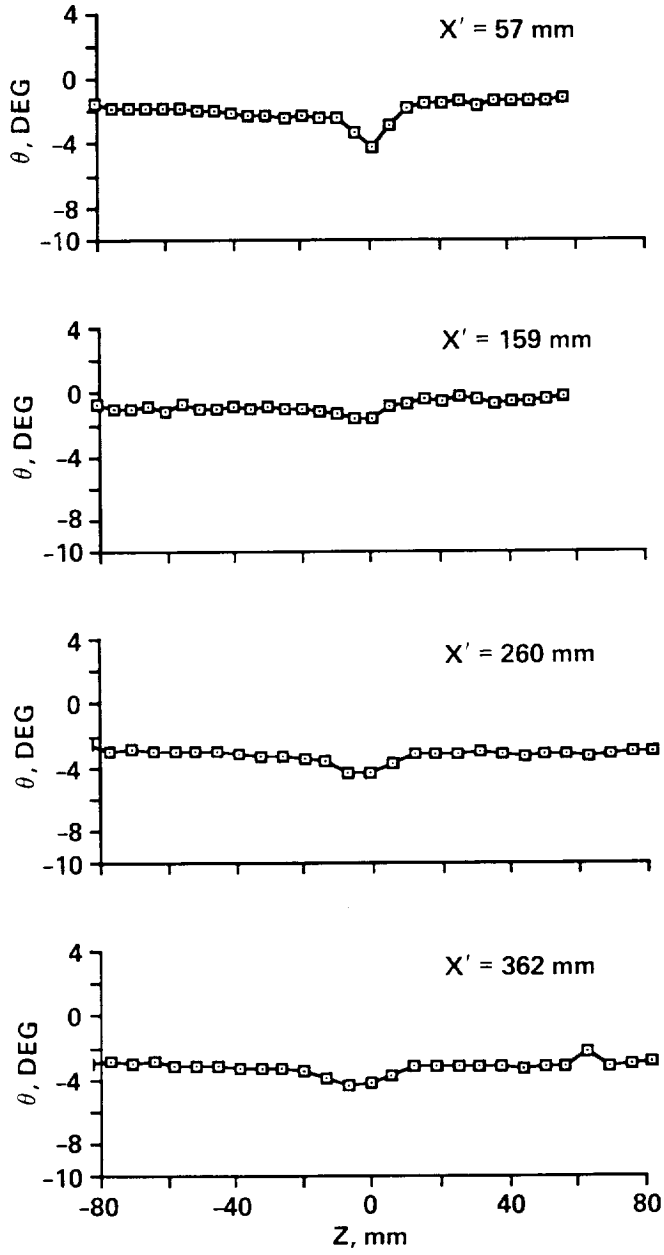

b) Pitch angle, θ, propeller off

Figure 20.– Continued.

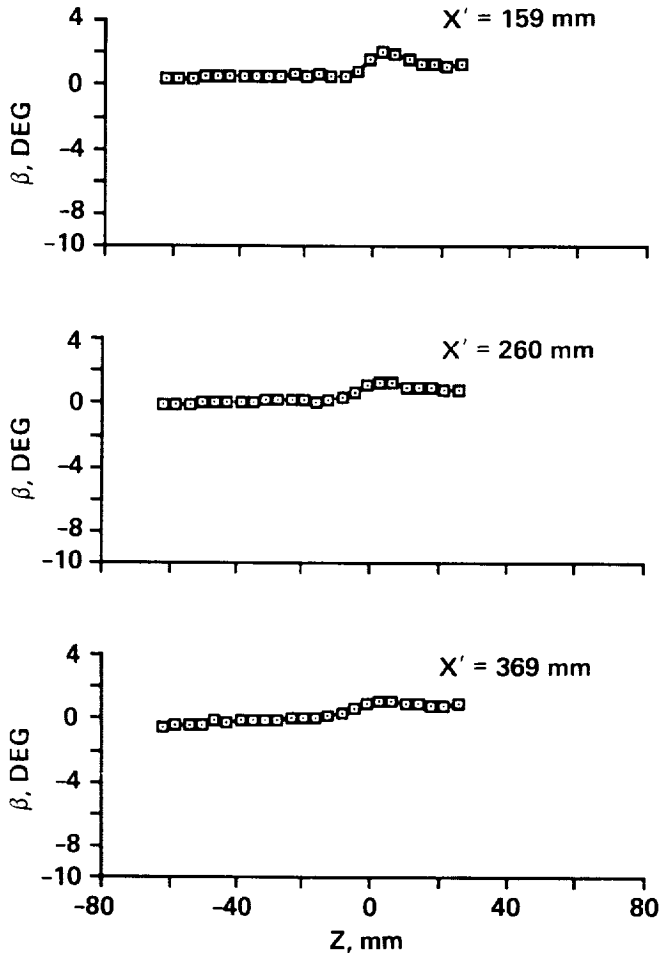

c) Yaw angle, ß, propeller operating.

Figure 20.– Continued.

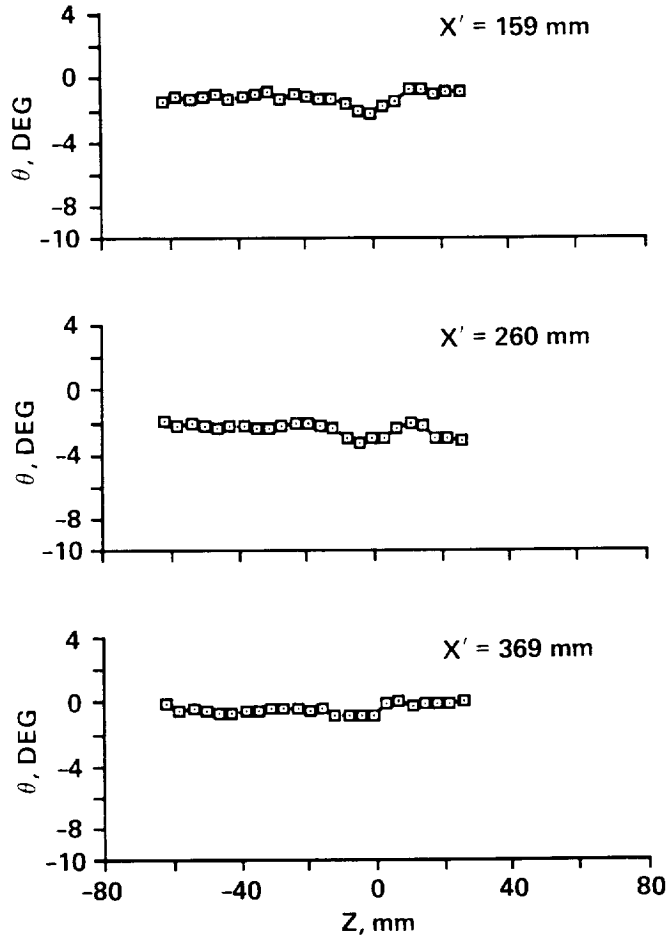

d) Pitch angle, θ, propeller operating.

Figure 20.– Concluded.

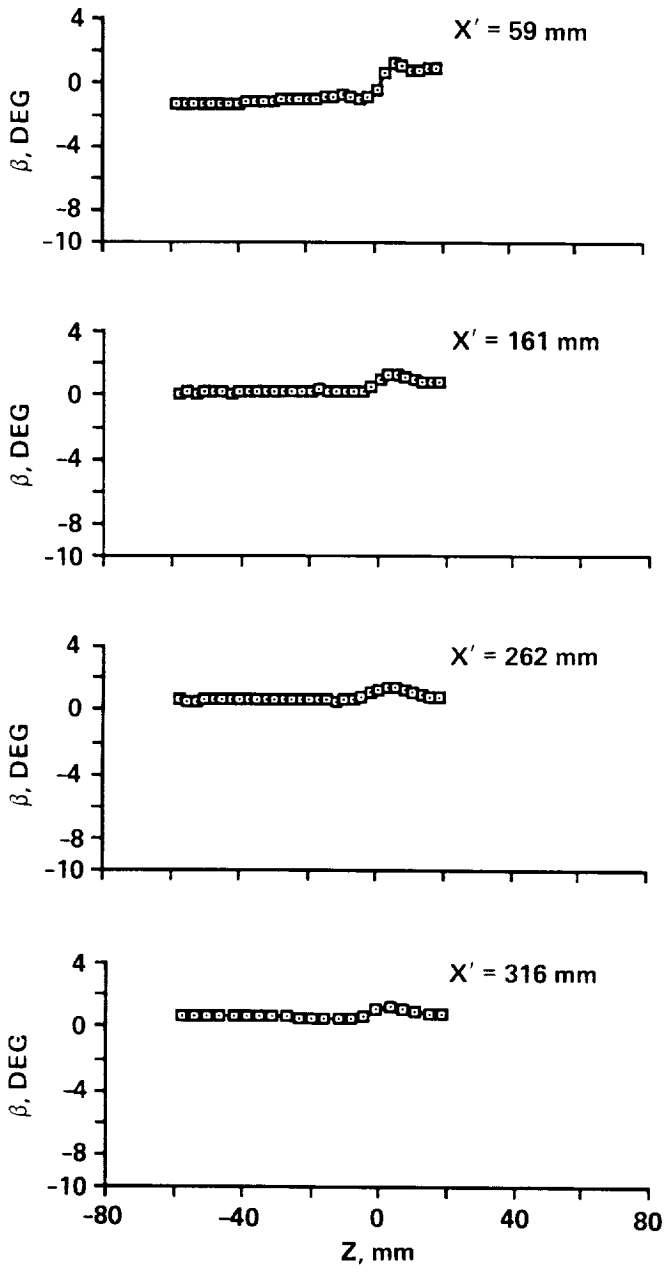

a) Yaw angle, ß, propeller off; Y = 305 mm

Figure 21.– Pitch and yaw angle distributions through the vertical tail fin wake - propeller off and propeller operating; Y = 305 and 311 mm.

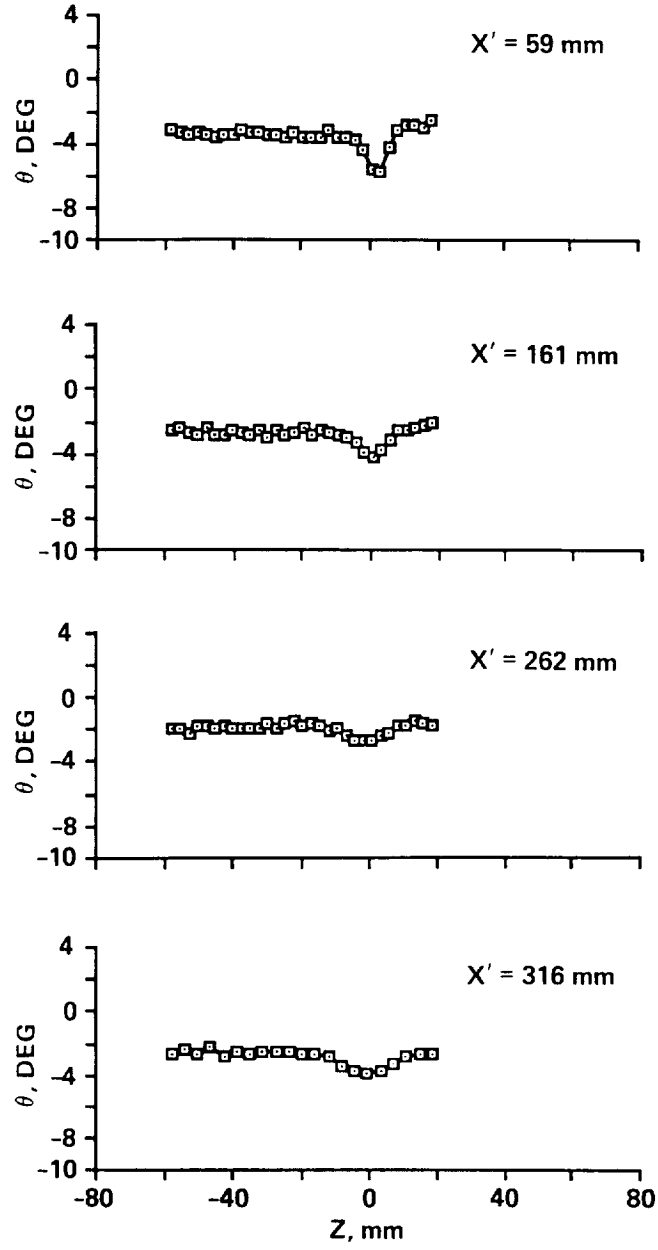

b) Pitch angle, θ, propeller off; Y = 305 mm

Figure 21.– Continued.

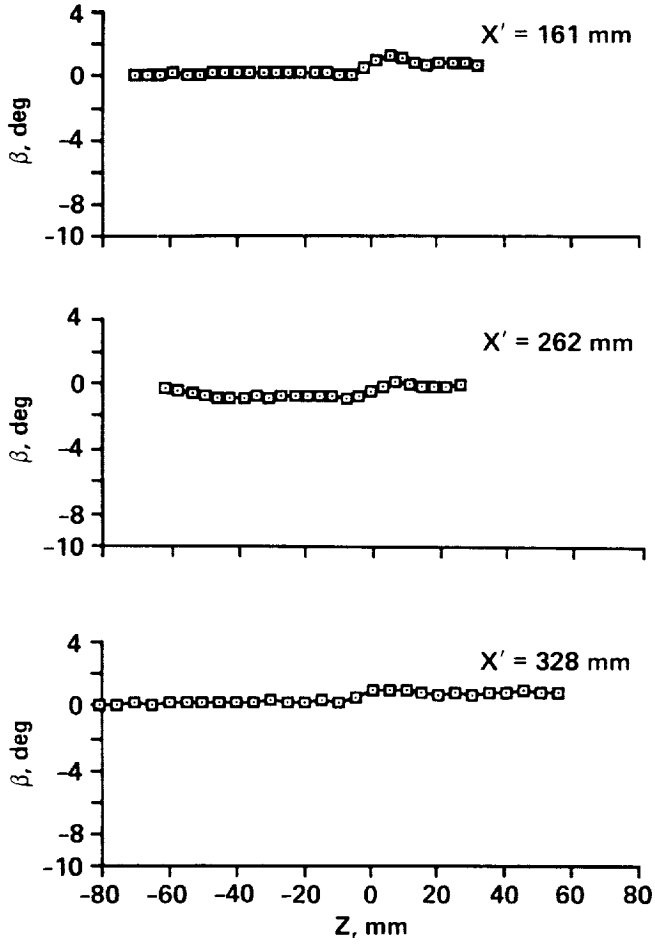

c) Yaw angle, ß, propeller operating; Y = 311 mm

Figure 21.– Continued.

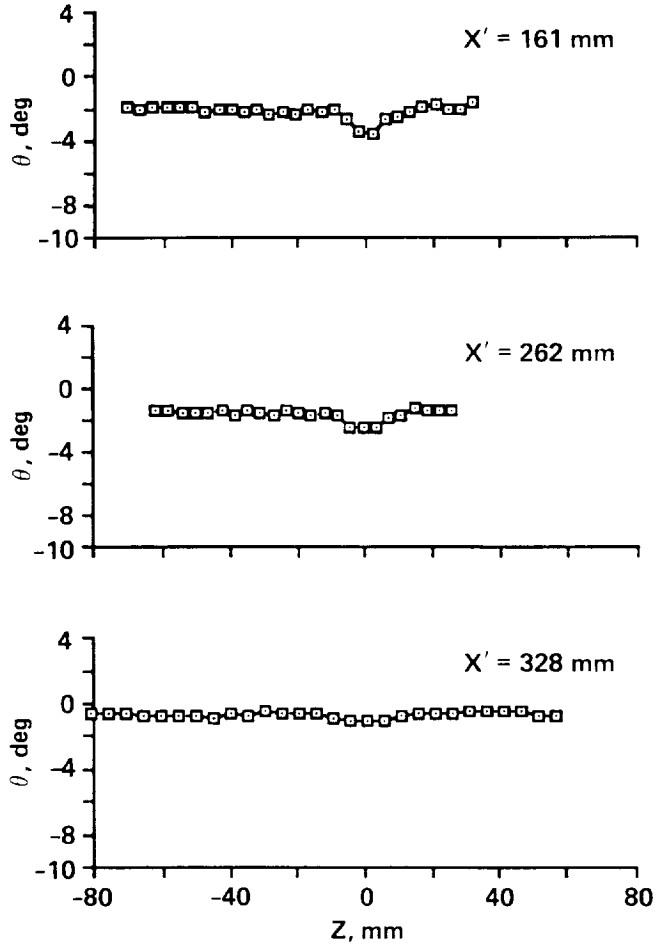

d) Pitch angle, θ, propeller operating; Y = 311 mm

Figure 21.– Concluded.

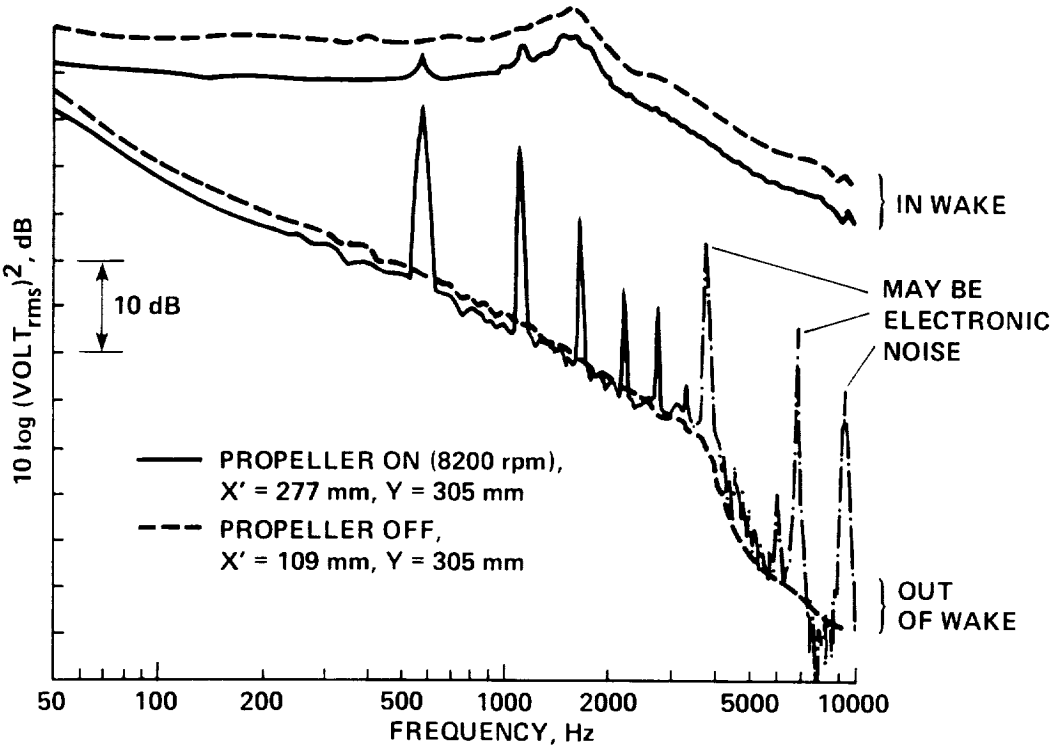

Figure 22.– Typical hot-wire spectra measured in and out of the vertical tail fin wake; 25 Hz constant bandwidth filters.

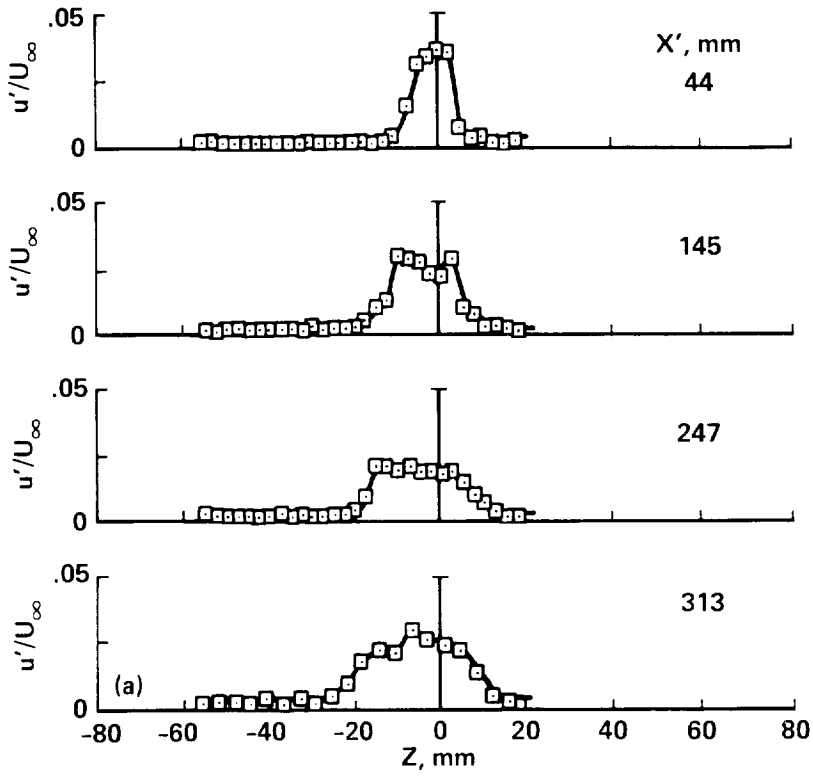

a) Propeller off, Y = 305 mm

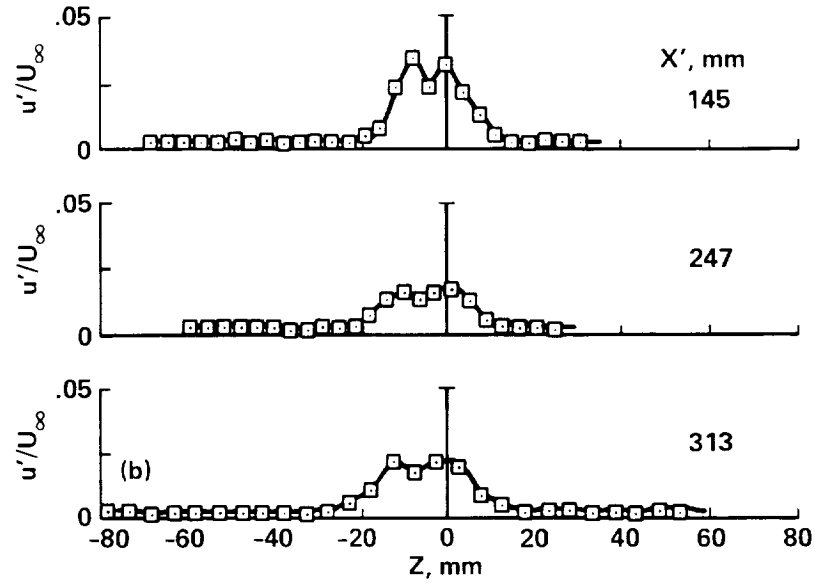

b) Propeller operating

Figure 23.– Surveys of streamwise turbulence, u'/U_∞, through the vertical tail fin wake - propeller off and propeller operating.

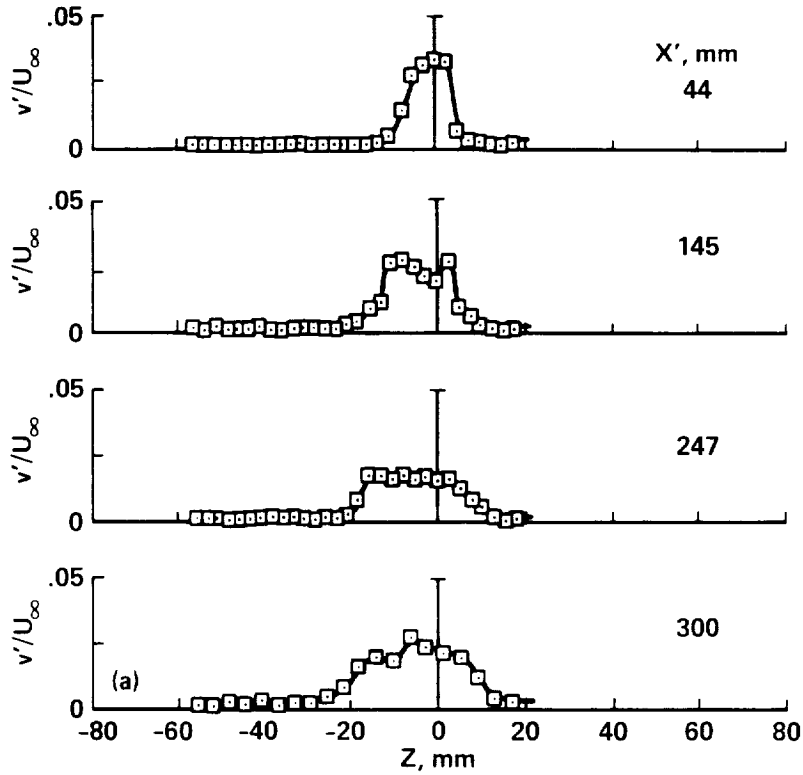

a) Propeller off, Y = 305 mm

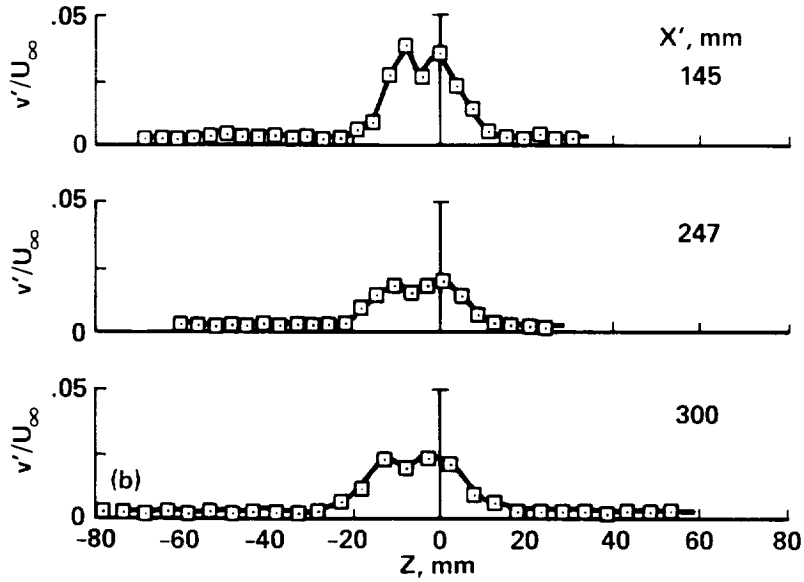

b) Propeller operating, Y = 310 mm

Figure 24.– Surveys of cross-stream turbulence, v'/U_∞, through the vertical tail fin wake - propeller off and propeller operating.

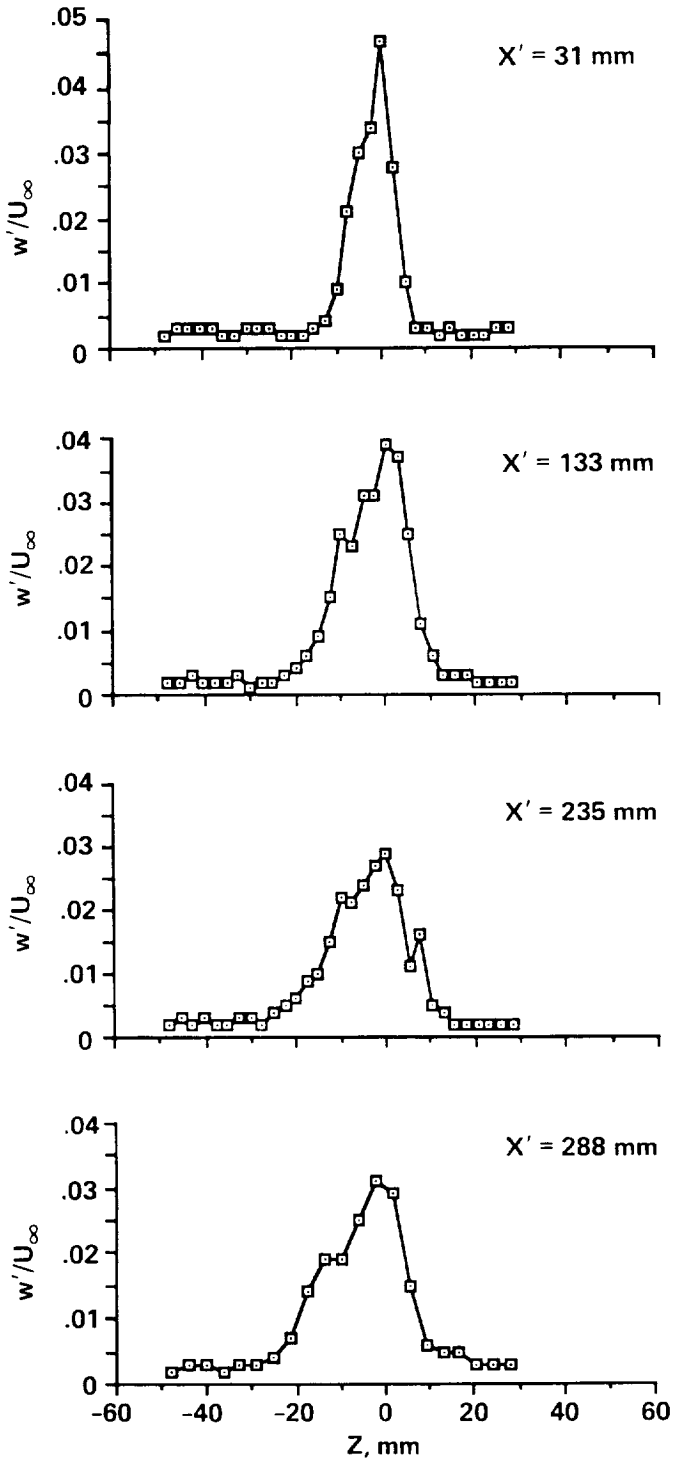

a) Propeller off, Y = 305 mm

Figure 25.– Surveys of cross-stream turbulence, w'/U_∞, through the vertical tail fin wake - propeller off and propeller operating.

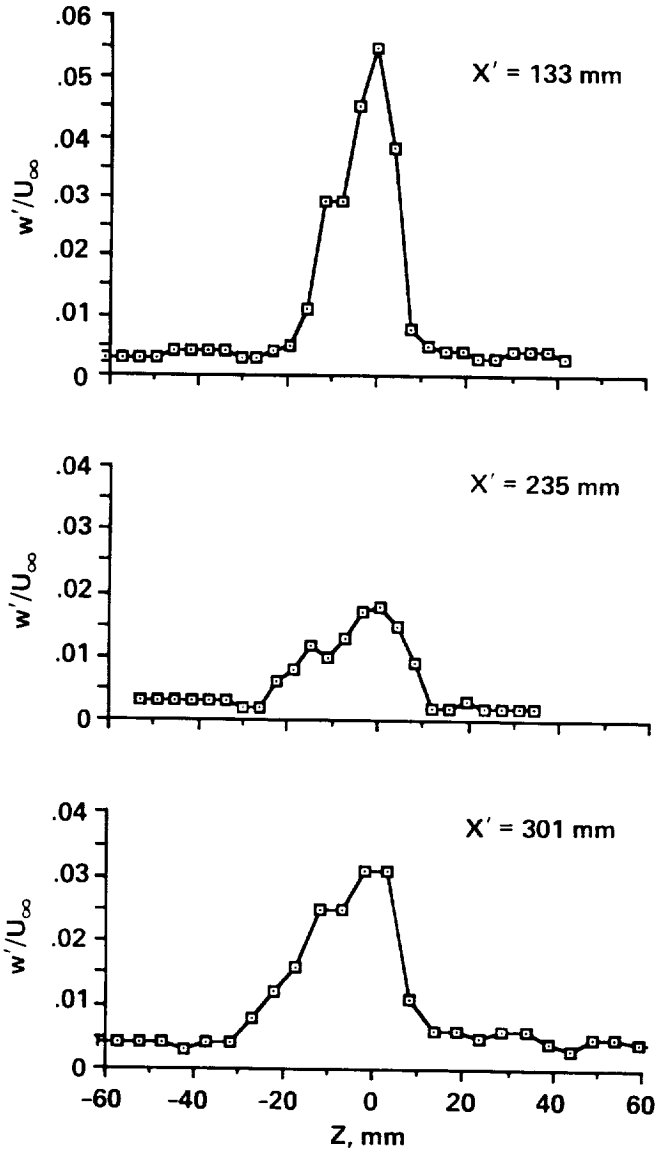

b) Propeller operating, Y = 308 mm

Figure 25.– Concluded.

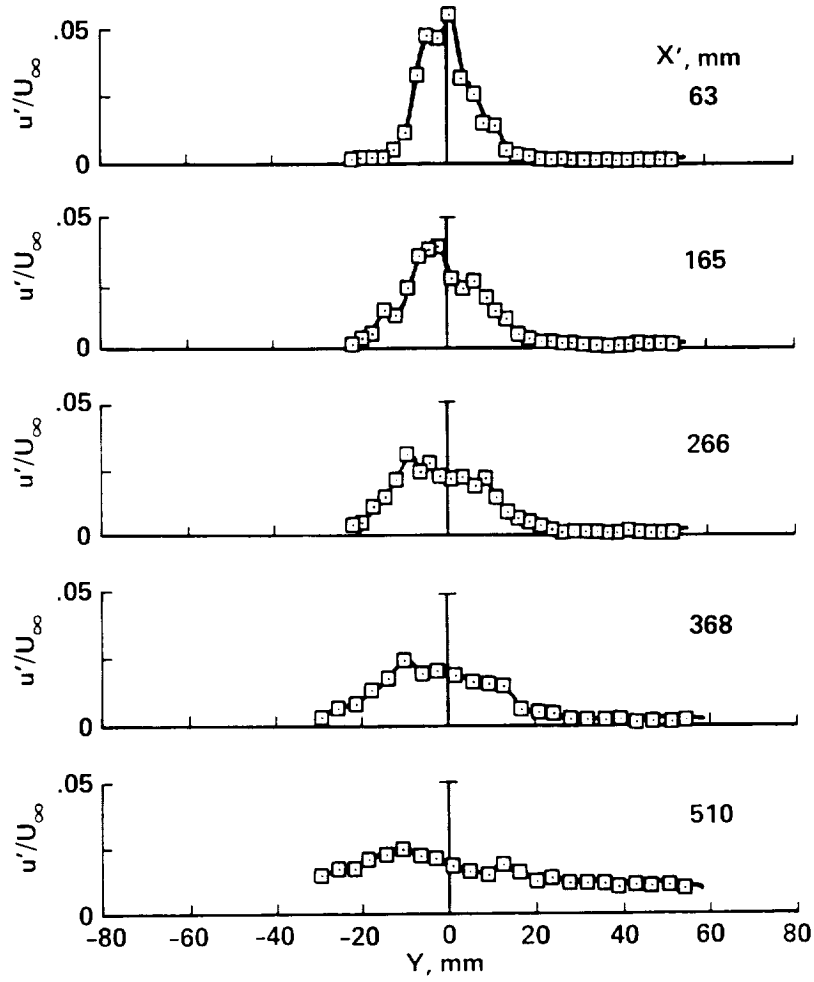

Figure 26.– Surveys of streamwise turbulence, u'/U_∞, through the Y-tail wake - propeller operating, Z = 160 mm.

NASA National Aeronautics and Space Administration

Report Documentation Page

1. Report No.	2. Government Accession No.	3. Recipient's Catalog No.
NASA TM-101003		

4. Title and Subtitle	5. Report Date
Flow-Field Survey of an Empennage Wake Interacting with a Pusher Propeller	October 1988
	6. Performing Organization Code

7. Author(s)	8. Performing Organization Report No.
W. Clifton Horne and Paul T. Soderman	A-88185
	10. Work Unit No.
	505-61-11

9. Performing Organization Name and Address	11. Contract or Grant No.
Ames Research Center Moffett Field, CA 94035	
	13. Type of Report and Period Covered
12. Sponsoring Agency Name and Address	Technical Memorandum
National Aeronautics and Space Administration Washington, DC 20546-0001	14. Sponsoring Agency Code

15. Supplementary Notes

Point of Contact: Paul T. Soderman, Ames Research Center, MS 247-2
Moffett Field, CA 94035 (415) 694-6675 or FTS 464-6675

16. Abstract

The flow field between a model empennage and a 591-mm-diameter pusher propeller was studied in the Ames 7- by 10-Foot Wind Tunnel with directional pressure probes and hot-wire anemometers. The region probed was bounded by the empennage trailing edge and downstream propeller. The wake properties, including effects of propeller operation on the empennage wake, were investigated for two empennage geometries: one, a vertical tail fin, the other, a Y-tail with a 34° dihedral. Results showed that the effect of the propeller on the empennage wake upstream of the propeller was not strong. The flow upstream of the propeller was accelerated in the streamwise direction by the propeller, but the empennage wake width and velocity defect were relatively unaffected by the presence of the propeller. The peak turbulence in the wake near the propeller tip station, 0.66 diameter behind the vertical tail fin, was approximately 3% of the free-stream velocity. The velocity field data can be used in predictions of the acoustic field due to propeller-wake interaction.

17. Key Words (Suggested by Author(s))	18. Distribution Statement
Aerodynamics Empennage wake Pusher propeller Wake turbulence Propeller-empennage interactions	Unclassified-Unlimited Subject Category - 01

19. Security Classif. (of this report)	20. Security Classif. (of this page)	21. No. of pages	22. Price
Unclassified	Unclassified	53	A04

For sale by the National Technical Information Service, Springfield, Virginia 22161